The Variation of Ionospheric O^+ and H^+ Outflow on Storm Timescales

N. Nowrouzi[1,2,†], L. M. Kistler[1,2], K Zhao[3], E. J. Lund[1], C. Mouikis[1], G. Payne[4], B. Klecker[5]

[1]Space Science Center, University of New Hampshire, Durham, NH, USA.
[2]Physics Department, University of New Hampshire, Durham, NH, USA.
[3]School of Mathematics and Statistics, Nanjing University of Information Science and Technology, Nanjing, China.
[4]University of Colorado Boulder.
[5]Max-Planck-Institut für extraterrestrische Physik, Garching, Germany.

Corresponding author: Niloufar Nowrouzi (nowrouzi@bu.edu)

†Now at Boston University.

Key Points:

- Both CME and SIR storms have their maximum O^+ and H^+ outflow during the main phase, and a decrease during the recovery phase.
- During CME storms, the outflow increases during the initial phase, while during SIR storms, it doesn't increase until the main phase.
- This difference in outflow timing may explain why more O^+ is observed in the ring current during CME storms than during SIR storms.

Abstract

Geomagnetic storms are primarily driven by stream interaction regions (SIRs) and coronal mass ejections (CMEs). Since SIR and CME storms have different solar wind and magnetic field characteristics, the magnetospheric response may vary accordingly. Using FAST/TEAMS data, we investigate the variation of ionospheric O^+ and H^+ outflow as a function of geomagnetic storm phase during SIR and CME magnetic storms. The effects of storm size and solar EUV flux, including solar cycle and seasonal effects, on storm time ionospheric outflow,

are also investigated. The results show that for both CME and SIR storms, the O^+ and H^+ fluence peaks during the main phase, and then declines in the recovery phase. However, for CME storms, there is also significant increase during the initial phase. Because the outflow starts during the initial phase in CME storms, there is time for the O^+ to reach the plasma sheet before the start of the main phase. Since plasma is convected into the ring current from the plasma sheet during the main phase, this may explain why more O^+ is observed in the ring current during CME storms than during SIR storms. We also find that outflow fluence is higher for large storms than moderate storms and is higher during solar maximum than solar minimum.

1 Introduction

There are two sources for the magnetospheric plasma: the solar wind and the ionosphere (Sharp, Johnson, & Shelley, 1974; Shelley et al., 1972). The solar wind consists predominantly of H^+ ions, with ~ 4% He^{++} ions and <1% other species. The ionospheric contribution mainly consists of H^+, the O^+ and N^+ group (indistinguishable in some instruments, and called O^+ in this paper) and He^+. Because H^+ can come from both sources, O^+ is often used as the tracer of ionospheric plasma. In addition, because of its higher mass and larger gyroradius, increased O^+ abundance can change the magnetospheric dynamics. The ionospheric outflow comes predominantly from the auroral oval, from the dayside cusp region around to the nightside auroral region. From the auroral regions, the ionospheric plasma is transported throughout the magnetosphere. The dayside outflow flows over the polar cap into the lobe, and can then enter the plasma sheet through reconnection. The nightside outflow has direct access to the near-earth plasma sheet. During geomagnetic storms, the plasma in the near-earth plasma sheet is driven into the inner magnetosphere by enhanced convection, where it forms the storm-time ring current.

Many previous studies have shown that the contribution of the ionospheric heavy ions to the magnetosphere tends to increase with geomagnetic activity at all locations along the transport path. During disturbed geomagnetic conditions, as identified by Kp and Dst indexes, the strength of ion outflow increases compared to quiet times, and the composition of ion outflow changes, with H^+ being dominant during quiet times and O^+ being dominant during active or storm times (Collin et al., 1984; Cully et al., 2003; Wilson et al., 2004; Yau et al., 1988). (Liao et

al. (2010) showed that the occurrence of O^+ beams in the polar caps and lobes, identified as the cusp-origin outflow, increases during geomagnetic storms. During storms, these ions enter the plasma sheet for many hours (Kistler et al., 2010). Young et al. (1982), Mouikis et al. (2010), and Maggiolo & Kistler (2014) have shown that the O^+ density in the plasma sheet increases with Kp.

For the ring current, Hamilton et al. (1988) and Greenspan & Hamilton, (2002) showed that the ionospheric heavy ion contribution to the ring current goes up during the main phase of a geomagnetic storm. Mouikis et al. (2019) separated geomagnetic storms into Coronal Mass Ejection (CME) driven storms and Stream Interaction Region (SIR) driven storms, and performed a superposed epoch analysis of the ring current O^+ and H^+ pressure as a function of geomagnetic storm phases. They reported a larger enhancement of the O^+ pressure, that is contributed mostly by the low-energy ions <~ 55 keV, during the main phase in CME storms than in SIR storms, while for the H^+ pressure, there is almost no significant difference between CME and SIR storms.

Outside of the ring current, while the general correlation with magnetic activity is established, the timing of the increased outflow relative to the phases of the storm has not been shown. The timing is critical because the O^+ outflow is relatively slow moving. For ionospheric ions to convect into the ring current during a storm main phase, they need to first travel to the near-earth plasma sheet. O^+ outflow from the cusp would take at least 2 hours (Kistler et al., 2019) to reach the plasma sheet. Nightside outflow will reach the nightside plasma sheet more quickly, but tends to be at lower energies, and so may not contribute significantly to the particle pressure that forms the ring current (Kistler et al., 2019). So, it remains an open question how the ionospheric ions are able to populate the pre-storm or main phase near-earth plasma sheet and get heated in time to be injected into the ring current during storm main phase.

To investigate this problem, this study uses a superposed epoch analysis of FAST data to examine how the ion outflow varies during a storm, addressing the differences between the two main drivers of geomagnetic storms, CMEs and SIRs. These two solar wind structures, on average have different solar wind and IMF characteristics when they impact the earth (Tsurutani et al., 2006). During the initial phase, CMEs often have an abrupt increase in ram pressure due to fast forward shocks. SIRs are usually not preceded by a shock at 1 AU, and have more

gradual onsets. CME structures often contain long-lasting southward IMF Bz. SIR structures usually have shorter excursions of southward IMF Bz, less sustained than for a CME. Because the CME and SIR solar wind structures and the amount of transported energy are different (Borovsky & Denton, 2006), it is likely that the ionospheric outflow driven by the structures will be different. The differences found by Mouikis et al. (2019) in the ring current may be due to differences in outflow fluence, or differences in outflow timing. Thus, for our study, we compare storms with the two drivers to identify the differences.

In addition to the storm drivers, the solar EUV flux may impact the outflow as well. Globally, solar EUV changes with the solar cycle, and locally, the incident EUV flux changes with the season. Yau, Beckwith et al. (1985), using DE-1 data, and Cully et al. (2003), using Akebono, showed that the occurrence of upflowing O^+ increased with F10.7, the proxy for Solar EUV, with a much smaller increase for H^+. The results for seasonal dependence are more mixed. Yau, Beckwith et al. (1985) observed that the O^+ outflow increased towards summer solstice. Peterson et al. (2006), on the other hand, using POLAR/TIMAS, found no systematic change in O^+ or H^+ outflow flux with season, although He^+ had a strong seasonal dependence. Collin et al. (1998) found a strong seasonal variation in the occurrence of upflowing beams, with more beams observed in the 1800-24:00 MLT sector during winter, but saw no change in the distribution of conics, and so the overall impact on outflow fluence may not be large. While solar EUV and season likely don't change the outflow on storm time-scales, they will impact the total fluence observed. Thus, we have also compared the outflow response of storms that occur during different phases of the solar cycle and under different seasons so that outflow rates under different conditions can be compared with other studies.

2 Instrumentation

To better understand auroral acceleration physics and magnetosphere-ionosphere coupling, the FAST satellite was launched in August 1996 into an elliptical polar orbit with a period of 133 minutes, an inclination angle of 83°, perigee of ~350 km, and apogee of ~ 4175 km (Charles W. Carlson, 1998). The FAST payload consists of six scientific instruments; the ElectroStatic Analyzers (ESAs) for gathering the electron (EESA) and ion (IESA) energy and pitch angle distributions (C W Carlson et al., 2001) the Time-of-flight Energy Angle Mass Spectrograph (TEAMS) instrument (Klumpar et al., 2001) to measure the 3-D distribution

functions of particle species H^+, O^+, He^+ and He^{++}, the Electric Field Sensors (Ergun et al., 2001) and the Magnetic Field Experiment sensors (Elphic et al., 2001) to measure the electric and magnetic fields data, respectively, and the Instrument Data Processor Unit (IDPU) to perform data processing.

In this paper, we use the recently released TEAMS L2 data to measure the ionospheric outflow and investigate the variation of ionospheric O^+ and H^+ outflow flux on storm timescales. The TEAMS L2 dataset includes a recalibration and a number of corrections. Over time, the TEAMS MCP efficiency degraded, with the amount of degradation depending on the position of the instrument positions (angular bins). In particular, the equatorial bins had very low efficiency. Using observations of plasma regions where assuming plasma gyrotropy is valid, the efficiencies of the individual positions were recalibrated using methods described in Kistler et al. (2013). Subsequently, a final cross-calibration with the IESA data set was performed that adjusted the overall level. A deadtime correction was also introduced that uses the IESA data, which is much less susceptible to deadtime, to determine the total count rate in the TEAMS instrument and applies a deadtime correction based on the count rate. The TEAMS measurement is corrected for spacecraft potential by shifting the distribution function, assuming the spacecraft charging is uniform around the spacecraft, and then the data is transformed to the convection frame (ExB frame) and sorted into pitch angle. Time periods when the spacecraft potential is less than -6V are excluded. Finally, time periods with incomplete data packets are flagged and excluded from the analysis.

3 Data Selection

3.1 Geomagnetic storms

To identify and characterize the storms, we used the Disturbance Storm-Time (Dst) index, upstream parameters including the z component of interplanetary magnetic field ($IMF\ B_z$), the solar wind pressure (P_{SW}), the solar wind density (n_{SW}), the solar wind speed (V_{SW}), and the geomagnetic and solar activity indices Auroral Electrojet (AE), the Kp index (multiplied by 10) and the F10.7 index. A sample plot of these parameters for the storm of May 15, 2005 is presented in Figure 1.

The storm phases were identified using the Dst index. We identified four critical times for each storm. Some storms have an initial phase that starts when the Dst rises sharply. This is usually caused by an increase in solar wind dynamic pressure. The vertical orange line indicates the increase time in Figure 1; this feature is not observable in all storms. The time when the Dst starts to drop is called the storm onset time and is shown with a vertical green line in Figure 1. The initial phase is the time between the Dst increase and the onset time. After onset, Dst decreases until it reaches the minimum value of Dst, shown with a red vertical line. The interval between onset and Dst minimum is called the main phase. IMF Bz is generally negative (southward) during this time. At the peak of the storm, the IMF Bz usually turns positive (northward). After the main phase, Dst increases back to zero in the recovery phase. For our study, we have included the time from Dst minimum to the time when the Dst index passes $\frac{1}{3} \times Dst_{minimum}$ or -20 nT, whichever is earlier, for the recovery phase. The vertical blue line shows the end of the recovery phase for this storm. In addition to these three storm phases, we defined a prestorm phase that extends from 24 hours before the initial phase to the initial phase. If there is no initial phase, the prestorm phase starts 27 hours before the onset and ends at the onset. In some cases, there are storms in close succession, such that the prestorm of the second storm overlaps with the first storm's recovery phase. To avoid double-counting data from the recovery phase in the prestorm phase, we added the condition that the Kp index must be less than 3 during the prestorm phase. With these definitions, we compiled a list of all geomagnetic storms that showed the classic storm profile (ie. a clear main phase and recovery phase) from solar cycle 23, from 1996 to 2009, that showed the classic storm profile (ie. a clear main phase and recovery phase). Storms with more complicated storm profiles, for which clear main and recovery phases could not be identified, were excluded. The minimum Dst index for the storms on the list is less than -50 nT.

We then identified the storm driver, CME or SIR, for each of these storms using previously published catalogs (Jian et al., 2006b, 2006a; Matamba & Habarulema, 2018; Richardson & Cane, 2010) and only used the storms with one identified driver in the study.

In Figure 2, the top panel shows the smoothed daily averaged F10.7 for solar cycle 23 and the bottom panel shows $Dst_{minimum}$ values for all identified storms used in the study. The red and blue symbols present the SIR and CME driven storms, respectively. As discussed in the

introduction, in addition to the solar wind driving conditions, the outflow flux also varies with solar EUV and possibly with solar illumination, represented by the season. Therefore, we divided the solar cycle into a solar minimum and a solar maximum phase using the F10.7 index of 150 (s.f.u) as the boundary. The minimum phase includes two sub-phases: descending and ascending phases. In Figure 2, the dotted vertical lines separate the solar cycle phases.

The FAST spacecraft data collection alternated between using northern hemisphere and southern hemisphere passes, and only rarely used both in the same orbit, so most storms include data from either the north or from the south. For data from the northern hemisphere, the summer season is from 03-22/00:00 to 09-22/00:00, and the winter season is from 09-22/00:00 to 03-22/00:00. For southern hemisphere data, the seasons are switched. The storms with TEAMS data from summer season are shown with triangles and from winter season with squares.

In Figure 2, the scatter plot of $Dst_{minimum}$ shows that the most intense storms occurred during the solar maximum phase and the first years of the declining phase. To study the effect of storm intensity on the ionospheric outflow, we divided the storms into two groups: moderate storms with $-150\ nT \leq Dst_{minimum} < -50\ nT$ and intense storm with $-150\ nT\ \geq Dst_{minimum}$. The horizontal dashed line in the bottom panel of Figure 2 indicates the separation of moderate and intense storms.

In Table 1. we list the total number of storms used in this analysis for each driver that fall into each category.

3.2 Ionospheric outflow flux

Equation 1 is used to calculate the ion outflow flux. In this equation, the variables α, E, and $j(m, E, \alpha)$ represent the pitch angle, energy, and energy flux data, respectively.

$$\Phi(m) = 2\pi \int_{E=10eV}^{E_{cutoff}} \int j(m, E, \alpha) |sin(\alpha) sin(\Delta\alpha) cos(\alpha) cos(\Delta\alpha)|\, dE d\alpha \quad \text{Equation 1}$$

For the energy integration, a lower energy threshold of 10 eV and a dynamic upper energy cutoff is used. The upper cutoff prevents the contribution of the magnetospheric precipitation population in the outflow flux calculation (Hatch et al., 2020; Zhao et al., 2020). To calculate the dynamic cutoff energy, we used the ratio of the upward (90° <pa <180°) and downward (270° < pa < 360°) flux from the iESA data at each energy for the northern

hemisphere. At any time, the cutoff energy is the highest energy with ratio ($\frac{flux_{upward}}{flux_{downward}}$) bigger than 2. If, at time t, the ratio never is bigger than 2, the cutoff energy is set to the minimum value, 10 eV, so there is no contribution to the flux. For this time, the eflux value corresponding to one count along the magnetic field direction is recorded.

A TEAMS summary plot of FAST orbit 8277, passing the noon-midnight of the northern hemisphere during the main storm phase, is shown in Figure 3. Panels (a), (b), and (c) contain the H^+ energy spectrogram, the H^+ pitch angle spectrogram plots for energies < 1 keV and the H^+ pitch angle spectrogram for energies > 1 keV, respectively. Panels (d), (e), and (f) present the corresponding spectrograms for O^+. Panel (g) shows the spacecraft's potential.

The black lines in panels (h) and (i) give the in-situ outflow flux for H^+ and O^+ species, which are calculated from Equation 1.

We normalize the net flux by mapping it to 300 km. The net outflow flux is inversely proportional to the cross-section of the flux tube, $\Phi \propto \frac{1}{A}$. On the other hand, the cross-section of the flux tube is inversely proportional to the magnitude of the magnetic field, $A \propto \frac{1}{B}$. At these altitudes, a dipole magnetic field is adequate for the mapping. The dipole magnetic field is inversely proportional to the third power of altitude, $B \propto \frac{1}{r^3}$. So, the net outflow flux is inversely proportional to the third power of altitude, $\Phi \propto \frac{1}{r^3}$.

The normalized net outflow flux, which we call outflow flux from now on, is plotted with the red line in panels (h) for H^+ and (i) for O^+. Also, the H^+ and O^+ outflow flux is plotted along the FAST trajectory in the dial plots located on the right side of panels (h) and (i) in Figure 3.

To determine how the outflow varies with the storm phase, we present the averaged outflow flux of H^+ and O^+ binned by MLT-ILAT. Only data above 1500 km altitude are included. Figure 4. shows an example of the data display we will use, in this case for O^+ during CME storms.

We divide the normalized net outflow flux by storm phase: prestorm, initial phase, main phase, and recovery phase (four columns). Four rows are shown: trajectory, all storms, moderate, and intense. The trajectory row shows the O^+ outflow flux along the spacecraft trajectory for each storm phase. The data is limited to Invariant Latitude (ILAT) greater than 50°; the circles

shown are in 10° increments. The next row shows all the storm data binned into 40 ILAT bins with a width of 1° and 24 magnetic local time (MLT) bins with a time width of 1 hour. The O^+ outflow flux measurements in each MLT-ILAT bin are averaged, and the averaged flux is assigned to the bin. The big circular plots show the averaged flux for each species. The smaller circular plots above each big plot show the number of data points associated with averaged flux of each MLT-ILAT bin in the smaller circular plots above the big plot. The third and fourth rows show the binned and averaged flux separately for the moderate and intense storms. Subsequently, we use these data to calculate the total fluence in four local time sectors.

4 Storm phases and storm intensity

4.1 O^+ outflow flux

Figure 4 shows the O^+ outflow data for CME storms. There is good coverage for all phases, with the highest number of data points for the recovery and prestorm phases. Because of the short duration of the storm initial phase, there are fewer data points from the initial phase. The all-storm panel shows that before the storm, there is a region of weak outflow in the cusp region, between ~70° and 85° invariant latitude and extending from 15MLT to 6 MLT. In the nightside sector, the weak outflow is also observed between 70° and 80° invariant latitudes. During the initial phase, the intensity of outflow flux increases and expands in both MLT and ILAT. The cusp shows the highest outflow, extending from 9 MLT to 17 MLT, with high outflow fluxes observed down to 67°. From 7 MLT to 9 MLT, the outflow reaches the lower latitude of 63°. The outflow flux on the nightside also increases, covering the latitude between 75° and 80°. During the main phase, the outflow flux increases significantly and is observed in all MLT regions. The coverage of high flux is between 60° and 80° invariant latitudes for dawnside and dayside and between 75° and 60° for duskside and nightside. In the recovery phase, the outflow flux decreases, with MLT-ILAT coverage similar to the main phase.

The next two rows compare the outflow from moderate and intense storms. As shown in Figure 2, we expect to have better statistics for moderate storms than intense storms. Comparing the O^+ outflow flux during moderate and intense storms shows that although the variation and spatial distribution of ionospheric O^+ outflow during storm phases are similar for both storm

intensity groups, intense storms drive higher O^+ outflow. The intense outflow is also occasionally observed down to 50° latitude.

Figure 5 shows the averaged O^+ outflow flux before and during the phases of SIR storms. In general, there are fewer SIR storms, therefor the MLT-ILAT coverage is not as good. From Table 1. we only have one intense SIR storm, so we limit our epoch analysis study to moderate SIR storms. Like the prestorm phase in CME storms, there is O^+ outflow flux before the storm, primarily at noon and after midnight. However, unlike the initial phase of CME storms, the flux does not increase significantly during the initial phase of SIR storms. Like CME storms, the maximum outflow flux occurs during the main phase and is observed in all MLT sectors. A distinct difference is that for or SIR's the maximum outflow is on the dawn side. The outflow does not generally extend as low in ILAT for SIR storms. In the recovery phase, the outflow flux declines, and the distribution is quite similar to the recovery phase of moderate CME storms.

The ion outflow rate (fluence) is a multiplication of the outflow flux and the surface area. Equation 2 gives the fluence emerged from the surface of bin jk.

$$fluence_{jk} = \left(\frac{\sum_{i=0}^{n_{jk}-1} \boldsymbol{flux_i}}{\boldsymbol{n_{jk}}}\right)_{\boldsymbol{jk}} \times A_{jk} \qquad \text{Equation 2}$$

Which $\left(\frac{\sum_{i=0}^{n_{jk}-1} \boldsymbol{flux_i}}{\boldsymbol{n_{jk}}}\right)_{\boldsymbol{jk}}$ is the averaged outflow flux, and A_{jk} is the area of bin jk. At a mapped altitude of 300 km, we calculated A_{jk} from Equation 3.

$$A_{jk} = -(\cos\theta_2 - \cos\theta_1)_j \times (\varphi_2 - \varphi_1)_k \times r^2 \qquad \text{Equation 3}$$

The radius r is the sum of mapped altitude and the Earth radius, in centimeters, $r = (R_E + 300) \times 10^5 \quad (cm)$.

We quantitatively illustrated the variation of ionospheric O^+ fluence during the CME and SIR storm phases separately by summing the fluences of all MLT-ILAT bins; For example, $fluence_{(dayside)} = \sum_{j=0,k=9}^{40,15} fluence_{jk}$

The line plots in Figure 6 show the variation of measured fluence for CME moderate storms with the solid red line, CME intense storms with the dashed red line, and SIR moderate storms with the solid blue line. Due to the low statistics of SIR intense storms, we do not include the fluence of SIR intense storms. The panels, from top to bottom give the total fluence covering

all MLT sectors, the (dusk + night) fluence measured from summing fluences of dusk and night side sectors, and the (dawn + day) fluence containing the fluences summed from dawnside and dayside bins. We have combined these sectors because we note that the dayside outflow tends to extend towards the dawn, while the nightside outflow extends towards the dusk. The error bars indicate the Standard Error of Mean (SEM).

We observe that the O^+ fluence before the storms are roughly the same for both CME and SIR storms. For CME storms, the fluence increases by a factor of 10 in the initial phase, increases further in the main phase, and declines in the recovery phase. For the SIR storms, the fluence is about the same in the initial phase, increases in the main phase and then decreases in the recovery phase.

Also, we observe that intense CME storms have more O^+ fluence than moderate CME storms. For moderate storms, the O^+ fluence produced during the main phase is about a factor of two higher in CME storms than in SIR storms. As stated earlier, the most significant difference between the fluence in CME moderate storms with SIR moderate storms is the O^+ fluence during the initial phase. The CME storms produce O^+ fluence 15 times higher than SIR storms in the initial phase. This significant difference is observed in both the "day + dawn" and "dusk + night" sectors.

4.2 H^+ Outflow flux

Figure 7 presents the averaged H^+ outflow flux during CME storms. Before the storm, the H^+ outflow was observed on both the dayside and nightside. As with the O^+, the H^+ outflow increased during the initial phase and extended in MLT and ILAT. The increased H^+ outflow reaches its maximum in the main phase, and it covers all MLT sectors with ILAT between 60° to 80°, even extending below 60° in a few bins. The flux declined in the recovery phase but still covers a wide MLT range. As with O^+, the H^+ flux is stronger and reaches a lower latitude in intense storms than in moderate storms. In large storms, the extended outflow down to 50 degrees in 18MLT and 6 MLT results from the auroral region.

Figure 8 shows the averaged H^+ outflow flux for SIR storms. The spatial distribution for the H^+ outflow for SIR storms is very similar to the O^+ outflow. As with O^+, there is essentially no increase during the initial phase. During the main phase, the strongest outflow is in the

dayside, while for O^+, it was on the dawnside, but it is still strong in both regions. As for O^+, the H^+ outflow is stronger and reaches a lower latitude during CME than during SIR storms.

The line plots in Figure 9 present the variation of total H^+ fluence as a function of storm phases during CME moderate (solid red line), CME intense (dashed red line), and SIR moderate (solid blue line) storms. The total fluence is almost the same in the prestorm phase. During the initial phase, the CME storms show a significant increase, while there is almost no increase for SIR moderate storms. In the main phase, the H^+ fluence produced by CME and SIR storms is about the same. In the Recovery phase, the moderate SIR storms had more H^+ fluence than CME moderate storms, and the fluxes are the same within the statistical error.

In the Recovery phase, the moderate SIR storms had more H^+ fluence than CME moderate storms; however, for "dusk + night" the CME flux is inside the SIR error bar.

Comparing CME moderate storms with SIR moderate storms shows that the total H^+ fluence during the initial phase of CME storms is significantly higher than during SIR storms, in both the dayside and the nightside sectors.

5. Solar cycle (solar EUV) and seasonal effects

After studying the effect of solar wind structures on ionospheric O^+ outflow, we investigate the impact of the solar cycle on storm time ionospheric O^+ outflow. We divided the moderate CME storms into two groups: solar maximum and solar minimum storms. The statistics of participating storms in this study are given in Table 1. First, we prepared the MLT-ILAT plots similar to Figure 4 and calculated the total fluence. Figures 10(a) and (b) depict the O^+ and H^+ fluences observed during moderate CME storms. The solid lines correspond to fluence levels recorded during solar maximum years, while the dashed lines represent fluence levels during solar minimum years. The fluences were computed separately for the (dusk + night) and (dawn + day) periods, as illustrated in the second and third panels from the top, respectively. Figures 10(c) and (d) illustrate the O^+ and H^+ fluences specifically observed during moderate CME storms restricted to solar minimum years. Here, the solid lines signify fluence levels recorded in the summer season, while the dashed lines indicate fluence levels in the winter season. The panel arrangement from top to bottom mirrors that of panels (a, b).

From Figure 10(a), it is clear that the total O^+ fluence is higher during solar maximum than during solar minimum. The difference is particularly noticeable during the main phase of storms, where it is 2.6 times higher. In Figure 10(b), it can be seen that the total H^+ fluence remains the same during both solar maximum and solar minimum. Furthermore, there is no difference in the (Day + Dawn) sector. However, in the (Dusk + Night) sector during solar minimum, more H^+ fluence is detected.

In Figure 10 (c, d), we present the measured O^+ and H^+ fluences from summer season (solid lines) and winter season (dashed lines) for CME solar minimum storms. From Figure 10(c), we find that the total O^+ fluence is stronger in summer than in winter. The separate panels for the (day + dawn) and (dusk + night) sectors show that the dayside O^+ fluence is stronger in the summer than in winter, while on the nightside, the O^+ fluence is almost independent of the season. Figure 10(d) shows that in contrast to O^+, the total H^+ fluence shows no overall change in the summer and winter seasons. However, on the nightside, the H^+ fluences are stronger in the winter than in summer, while on the dayside, the H^+ fluence is stronger in the summer than in winter.

6. Discussion

The observation that the outflow increases during the initial phase for CME storms, both on the dayside and the nightside, may explain the higher O^+ observed during CME storms by Mouikis et al. (2019). CMEs are often preceded by a shock with enhanced dynamic pressure. Auroral effects from enhanced dynamic pressure have been observed previously. Brittnacher et al. (2000) show an example where the arrival of the pressure enhancement associated with a CME was observed in the aurora, with the intensification first observed on the dayside, with a nightside enhancement observed 15 minutes later. Boudouridis et al. (2003) found that the response of the size and strength of the auroral oval to a pressure enhancement was global, with a noon-midnight propagation of the effect observed for cases when the IMF is northward. Simulations indicate that enhanced dynamic pressure increases energy input to the aurora from precipitating electrons (Damiano et al., 2010), which would drive the enhanced outflow. O^+ outflow during the initial phase has time to convect from the dayside to the nightside plasma sheet before the enhanced convection, associated with the storm main phase, begins. That outflow from enhanced dynamic pressure may populate the plasmasheet prior to a storm was

373 shown by (Kistler et al., 2016). They observed the flux of hot, energetic (~ 5 keV) O^+ ions in the
374 plasma sheet increase after a large pressure pulse hit the Earth's magnetosphere but before the
375 start of the storm main phase. The hot O^+ in the plasma sheet also preceded the observation of O^+
376 outflow coming directly from the nightside aurora. The inward convection of the hot O^+ from the
377 prestorm plasma sheet dominated the ring current pressure during the storm main phase.

378 It is also possible that differences in the main phase outflow fluence, between CMEs and
379 SIRs, play a role in making the ring current during CMEs richer in O^+. The outflow fluence of
380 O^+ during moderate CME storms is about a factor of two higher than the fluence during SIR
381 storms, while the H^+ fluence is about the same. This will lead to a higher O^+ abundance
382 throughout the magnetosphere.

383 The observed variations with solar cycle agree with the schematic model of Yau et al.
384 (1985) and Yau et al. (1988) in which an upward shift of the ionospheric O^+ source region from
385 solar minimum to solar maximum causes a correlation between increasing ionospheric O^+
386 density and increasing F10.7 in quiet and active times. The O^+ variation with storm phase is
387 about the same during solar minimum and solar maximum, but the O^+ fluence is higher during
388 all phases. The H^+ fluence showed no change between solar maximum and minimum phases on
389 the dayside, but on the nightside, more H^+ fluence is seen during solar minimum than the solar
390 maximum.

391 Our study of the seasonal effect on storm-time ionospheric outflow was limited to the
392 solar minimum phase (ascending and declining phases) of solar cycle 23. For the nightside
393 sector, O^+ fluence is independent of season. On the dayside, the CME storm time O^+ fluence is
394 stronger during the summer season than the winter season, in agreement with the Yau, Beckwith
395 et al. (1985) result. However, on the nightside, there was no difference. For H^+, the nightside
396 fluence is stronger during the winter season than in the summer season. For the dayside, H^+
397 fluence showed no seasonal effect. The stronger nightside fluence during winter may be a result
398 of the enhanced energetic electron precipitation in the nightside region during winter (Newell et
399 al., 1996) and is consistent with the observation of more ion beams in winter than in summer
400 (Collin et al., 1998).

401 In this study, the net ionospheric H^+ and O^+ fluences were significantly less than
402 observations from other studies (Collin et al., 1984; Cully et al., 2003; Peterson et al., 2001; Yau

et al., 1988). These studies were done with different instruments on different spacecraft at different altitudes and under various geomagnetic and solar cycle conditions. To have a better understanding of this discrepancy, Table 2. lists the instrumental and geomagnetic features of studies in addition to the reported H^+ and O^+ fluences.

In the column labeled "this study", we report the FAST total averaged fluences for H^+ and O^+ from the region with ILAT greater than 50°, the altitude range of 1500 km to 4200 km, and the energy range of 10 eV/e to 12000 eV/e, for prestorm times, as quiet time, and for moderate CME and SIR storms. Since our observation showed that ionospheric outflow is impacted by the solar cycle, the fluences during the solar maximum and the solar minimum phases are separated in Table 2. The next columns indicate the information from Table 1. of the Collin et al. (1984) study, Figure 3. in Yau et al. (1988), Table 5. in Peterson et al. (2001), and Figure 3. in Cully et al. (2003).

In Figure 11, the H^+ and O^+ outflow rates from the quiet time during solar minimum from different spacecraft are plotted as a function of altitude. From the plot, we see that the DE-1 spacecraft from the highest altitude reported the highest values, and the FAST spacecraft with the lowest altitude reported the lowest values for H^+ and O^+ rates. Thus one possibility for the discrepancies is that the ions are continuously accelerated as they move up the field line and therefore, cold ions that are invisible at lower altitudes move above the low-energy instrument threshold at higher altitudes. However, the four instruments all have different low-energy thresholds, and therefore some results do not support this picture. The instrument on S3-3 had a lower energy threshold of 500 eV, significantly higher than the other instruments. In fact, as seen in the example in Figure 4, most of the outflow observed in this study is below 500 eV. The high values reported by (Cully et al., 2003) may therefore be due to difficulties in subtracting the upflow contribution of precipitating particles, a problem avoided in this study by using the dynamic high energy cut-off. The Akebono/SMS has the lowest energy threshold, of 1 eV, but also the lowest high-energy threshold, 70 eV. Thus, the agreement with FAST for O^+ may be due to measuring the outflow with a higher contribution of low energies, and less contribution of higher energies. The large difference between the FAST measurements and Akebono for H^+ indicates a significant contribution below 10 eV. The better agreement between Akebono and Polar with DE-1 for H^+ than for O^+ may indicate that the majority of the H^+ reaches detectable energies at a lower altitude than the O^+. Still, the many differences between the different data

sets make it impossible to completely reconcile the discrepancies in the total fluence measurements.

7. Summary Conclusion

In this paper, we performed a comprehensive analysis to determine the variation of ionospheric O^+ and H^+ outflow as a function of geomagnetic storm for CME and SIR storms. We used FAST and OMNI data from 1996 to 2008, covering the solar cycle 23. In this period, 139 geomagnetic storms with Dst < -50nT were identified that had good FAST data coverage and were driven by clear CME or SIR solar wind structures. We excluded storms with undetermined drivers and storms with complex drivers. We found that:

1- O^+ and H^+ outflows increase in the initial phase of CME storms but do not increase until the main phase in SIR storms; For CME storms, the outflow in the initial phase has time to reach the plasma sheet prior to the main phase, and therefore may explain why CME storms have more O^+ than SIR storms.

2- in both CME and SIR storms, the maximum outflow occurs in the main phase and then declines in the recovery phase.

3- In dividing the storms by Dst, intense CME storms (Dst <-150) produce more O^+ and H^+ outflow than moderate storms (Dst>-150).

4- The O^+ outflows produced by moderate CME are slightly larger than SIR storms during main phase and comparable in the recovery phases. The H^+ is comparable during all phases.

5- O^+ outflow increases with increasing solar EUV flux, while H^+ outflow in the dayside is independent of solar EUV flux while in the nightside decreases with increasing solar EUV.

6- Dayside O^+ and H^+ outflows increase in summer season. The nightside O^+ outflow is independent of the season, while the nightside H^+ outflow increases in winter.

7- The differences between the FAST O^+ and H^+ total fluence with measurements from DE-1 by Yau et al. (1988) suggest that the FAST measurements, with a low energy cutoff of 10 eV, do not represent the total outflow flux. It is likely that O^+ and H^+ continue to be energized at altitudes above the FAST spacecraft.

Acknowledgements

The work at the University of New Hampshire was supported by the National Aeronautics and Space Administration under grants 80NSSC19K0073, 80NSSC20K0594, NNX15AQ91G, NSF 1502937, 80NSSC19K0363. The FAST(TEAMS) data are available via https://spdf.gsfc.nasa.gov/pub/data/fast/teams/l2/pa/

References

Borovsky, J. E., & Denton, M. H. (2006). Differences between CME-driven storms and CIR-driven storms. *Journal of Geophysical Research: Space Physics*, *111*(7). https://doi.org/10.1029/2005JA011447

Boudouridis, A., Zesta, E., Lyons, L. R., Anderson, P. C., Lummerzheim, D., & Boudouridis, C. : (2003). Effect of solar wind pressure pulses on the size and strength of the auroral oval. *Journal of Geophysical Research*, *108*(A4), 8012. https://doi.org/10.1029/2002JA009373

Brittnacher, M., Wilber, M., Fillingim, M., Chua, D., Parks, G., Spann, J., & Germany, G. (2000). Global auroral response to a solar wind pressure pulse. *Advances in Space Research*, *25*(7–8), 1377–1385. https://doi.org/10.1016/S0273-1177(99)00647-X

Carlson, C W, Mcfadden, J. P., Turin, P., Curtis, D. W., & Martin, L. (2001). The electron and ion plasma experiment for FAST. *Space Science Reviews*, *98*, 33–66.

Carlson, Charles W. (1998). The Fast Auroral Snapshot Explorer. *Geophysical Research Letters*, *25*(12), 2013–2016. https://doi.org/10.1029/91EO00202

Collin, H. L., Sharp, R. D., & Shelley, E. G. (1984). The magnitude and composition of the outflow of energetic ions from the ionosphere. *Journal of Geophysical Research*, *89*(A4), 2185–2194. https://doi.org/10.1029/JA089iA04p02185

Collin, H. L., Peterson, W. K., Lennartsson, O. W., & Drake, J. F. (1998). The seasonal variation of auroral ion beams. *Geophysical Research Letters*, *25*(21), 4071–4074. https://doi.org/10.1029/1998GL900090

Cully, C. M., Donovan, E. F., Yau, A. W., & Arkos, G. G. (2003). Akebono/suprathermal mass spectrometer observations of low-energy ion outflow: Dependence on magnetic activity and solar wind conditions. *Journal of Geophysical Research: Space Physics*, *108*(A2). https://doi.org/10.1029/2001JA009200

Damiano, P. A., Brambles, O. J., Lotko, W., Zhang, B., Wiltberger, M., & Lyon, J. (2010). Effects of solar wind dynamic pressure on the ionospheric O + fluence during the 31 August

2005 storm. *Journal of Geophysical Research*, *115*, 0–07. https://doi.org/10.1029/2010JA015583

Elphic, R. C., Means, J. D., Snare, R. C., Strangeway, R. J., Kepko, L., & Ergun, R. E. (2001). Magnetic field instruments for the Fast Auroral Snapshot Explorer. *Space Science Reviews*, *98*, 151–168.

Ergun, R. E., Carlson, C. W., Mozer, F. S., Delory, G. T., Temerin, M., Mcfadden, J. P., et al. (2001). The FAST satellite fields instruments. *Space Science Reviews*, *98*, 67–91.

Greenspan, M. E., & Hamilton, D. C. (2002). Relative contributions of H<supscr>+</supscr> and O<supscr>+</supscr> to the ring current energy near magnetic storm maximum. https://doi.org/10.1029/2001JA000155

Hamilton, D. C., Gloeckler, G., Ipavich, F. M., Stüdemann, W., Wilken, B., & Kremser, G. (1988). Ring current development during the great geomagnetic storm of February 1986. *Journal of Geophysical Research*, *93*(A12), 14343. https://doi.org/10.1029/ja093ia12p14343

Hatch, S. M., Moretto, T., Lynch, K. A., Laundal, K. M., Gjerloev, J. W., & Lund, E. J. (2020). The relationship between cusp region ion outflows and east-west magnetic field fluctuations at 4000-km altitude. *Journal of Geophysical Research: Space Physics*, *125*(3). https://doi.org/10.1029/2019JA027454

Jian, L., Russell, C. T., Luhmann, J. G., & Skoug, R. M. (2006a). Properties of interplanetary coronal mass ejections at one AU during 1995 - 2004. *Solar Physics*, *239*(1–2), 393–436. https://doi.org/10.1007/s11207-006-0133-2

Jian, L., Russell, C. T., Luhmann, J. G., & Skoug, R. M. (2006b). Properties of stream interactions at one AU during 1995 - 2004. *Solar Physics*, *239*(1–2), 337–392. https://doi.org/10.1007/s11207-006-0132-3

Kistler, L. M., Mouikis, C. G., Klecker, B., & Dandouras, I. (2010). Cusp as a source for oxygen in the plasma sheet during geomagnetic storms. *Journal of Geophysical Research: Space Physics*, *115*(3). https://doi.org/10.1029/2009JA014838

Kistler, L. M., Mouikis, C. G., & Genestreti, K. J. (2013). In-flight calibration of the Cluster/CODIF sensor. *Geoscientific Instrumentation, Methods and Data Systems*, *2*(2), 225–235. https://doi.org/10.5194/gi-2-225-2013

Kistler, L. M., Mouikis, C. G., Spence, H. E., Menz, A. M., Skoug, R. M., Funsten, H. O., et al. (2016). The source of O+ in the storm time ring current. *Journal of Geophysical Research: Space Physics*, *121*(6), 5333–5349. https://doi.org/10.1002/2015JA022204

Kistler, L. M., Mouikis, C. G., Asamura, K., Yokota, S., Kasahara, S., Miyoshi, Y., et al. (2019). Cusp and nightside auroral sources of O+ in the plasma sheet. *Journal of Geophysical Research: Space Physics*, *124*(12), 10036–10047. https://doi.org/10.1029/2019JA027061

Klumpar, D. M., Möbius, E., Kistler, L. M., Popecki, M., Hertzberg, E., Crocker, K., et al. (2001). The Time-of-flight Energy, Angle, Mass Spectrograph (TEAMS) experiment for FAST. *Space Science Reviews*, *98*(1–2), 197–219. https://doi.org/10.1023/A:1013127607414

Liao, J., Kistler, L. M., Mouikis, C. G., Klecker, B., Dandouras, I., & Zhang, J. C. (2010). Statistical study of O+ transport from the cusp to the lobes with Cluster CODIF data. *Journal of Geophysical Research: Space Physics*, *115*(12). https://doi.org/10.1029/2010JA015613

Maggiolo, R., & Kistler, L. M. (2014). Spatial variation in the plasma sheet composition: Dependence on geomagnetic and solar activity. *Journal of Geophysical Research: Space Physics*, *119*(4), 2836–2857. https://doi.org/10.1002/2013JA019517

Matamba, T. M., & Habarulema, J. B. (2018). Ionospheric responses to CME- and CIR-driven geomagnetic storms along 30°E–40°E over the African sector from 2001 to 2015. *Space Weather*, *16*(5), 538–556. https://doi.org/10.1029/2017SW001754

Mouikis, C. G., Kistler, L. M., Liu, Y. H., Klecker, B., Korth, A., & Dandouras, I. (2010). H+ and O+ content of the plasma sheet at 15-19 Re as a function of geomagnetic and solar activity. *Journal of Geophysical Research: Space Physics*, *115*(12). https://doi.org/10.1029/2010JA015978

Mouikis, C. G., Bingham, S. T., Kistler, L. M., Farrugia, C. J., Spence, H. E., Reeves, G. D., et al. (2019). The storm-time ring current response to ICMEs and CIRs Using Van Allen Probe observations. *Journal of Geophysical Research: Space Physics*, *124*(11), 9017–9039. https://doi.org/10.1029/2019JA026695

Newell, P. T., Feldstein, Y. L., Galperin, Y. I., & Meng, C.-I. (1996). Correction to “Morphology of nightside precipitation” by Patrick T. Newell, Yasha I. Feldstein, Yuri I. Galperin, and

Ching-I. Meng. *Journal of Geophysical Research: Space Physics*, *101*(A8), 17419–17421. https://doi.org/10.1029/96ja02055

Peterson, W. K., Coilin, H. L., Yau, A. W., & Lennartsson, O. W. (2001). Polar/Toroidal imaging mass-angle spectrograph observations of suprathermal ion outflow during solar minimum conditions. *Journal of Geophysical Research: Space Physics*, *106*(4), 6059–6066. https://doi.org/10.1029/2000ja003006

Peterson, W. K., Collin, H. L., Lennartsson, O. W., & Yau, A. W. (2006). Quiet time solar illumination effects on the fluxes and characteristic energies of ionospheric outflow. *Journal of Geophysical Research: Space Physics*, *111*(11). https://doi.org/10.1029/2005JA011596

Richardson, I. G., & Cane, H. v. (2010). Near-earth interplanetary coronal mass ejections during solar cycle 23 (1996 - 2009): Catalog and summary of properties. *Solar Physics*, *264*(1), 189–237. https://doi.org/10.1007/s11207-010-9568-6

Sharp, R. D., Johnson, R. G., Shelley, E. G., & Harris, K. K. (1974). Energetic O+ ions in the magnetosphere. *Journal of Geophysical Research*, *79*(13), 1844–1850. https://doi.org/10.1029/ja079i013p01844

Sharp, R. D., Johnson, R. G., & Shelley, E. G. (1974). Satellite measurements of auroral alpha particles. *Journal of Geophysical Research*, *79*(34), 5167–5170. https://doi.org/10.1029/ja079i034p05167

Shelley, E. G., Johnson, R. G., & Sharp, R. D. (1972). Satellite observations of energetic heavy ions during a geomagnetic storm. *Journal of Geophysical Research*, *77*(31), 6104–6110. https://doi.org/10.1029/ja077i031p06104

Tsurutani, B. T., McPherron, R. L., Gonzalez, W. D., Lu, G., Gopalswamy, N., & Guarnieri, F. L. (2006). Magnetic storms caused by corotating solar wind streams. In *Geophysical Monograph Series* (Vol. 167, pp. 1–17). Blackwell Publishing Ltd. https://doi.org/10.1029/167GM03

Wilson, G. R., Ober, D. M., Germany, G. A., & Lund, E. J. (2004). Nightside auroral zone and polar cap ion outflow as a function of substorm size and phase. *Journal of Geophysical Research: Space Physics*, *109*(A2), 1–18. https://doi.org/10.1029/2003JA009835

Yau, A. W., Shelley, E. G., Peterson, W. K., & Lenchyshyn, L. (1985). Energetic auroral and polar ion outflow at DE 1 altitudes: Magnitude, composition, magnetic activity dependence,

584 and long-term variations. *Journal of Geophysical Research*, *90*(A9), 8417.
585 https://doi.org/10.1029/ja090ia09p08417
586 Yau, A. W., Beckwith, P. H., Peterson, W. K., & Shelley, E. G. (1985). Long-term (solar cycle)
587 and seasonal variations of upflowing ionospheric ion events at DE1 altitudes. *Journal of*
588 *Geophysical Research*, *90*(A7), 6395. https://doi.org/10.1029/ja090ia07p06395
589 Yau, A. W., Peterson, W. K., & Shelley, E. G. (1988). Quantitative parametrization of energetic
590 ionospheric ion outflow. *American Geophysical Union*, 211–217.
591 https://doi.org/10.1029/gm044p0211
592 Young, D. T., Balsiger, H., & Geiss, J. (1982). Correlations of magnetospheric ion composition
593 with geomagnetic and solar activity. *Journal of Geophysical Research*, *87*(A11), 9077.
594 https://doi.org/10.1029/ja087ia11p09077
595 Zhao, K., Kistler, L. M., Lund, E. J., Nowrouzi N., Kitamura, N., & Strangeway, R. J. (2020).
596 Factors controlling O+ and H+ outflow in the cusp during a geomagnetic storm:
597 FAST/TEAMS observations. *Geophysical Research Letter*, *47*(11).
598 https://doi.org/10.1029/2004JA010829
599

600 **Tables**

601 *Table 1. Geomagnetic storms with identified drivers from 1996 to 2008.*

602

	TOTAL	CME	SIR
total storms	139	104	35
intense storm(I-storms)	27	26	1
moderate storm(M-storms)	112	78	34
M-storm in maximum phase	45	37	8
		Summer: 15	Summer: 4
		Winter: 21	Winter: 3
		Summer and winter: 1	Summer and winter: 1
M- storm in minimum phase	67	41	26
		Summer: 15	Summer: 11
		Winter: 20	Winter: 14
		Summer and winter: 6	Summer and winter: 1

603 *Table 2. Comparing the total H^+ and O^+ fluences scaping from ionosphere in different studies.*

			This Study[1]	Collin[2]	Yau[3]	Peterson[4]	Cully[5]
Spacecraft			FAST (TEAMS)	S3-3 (Lockheed)	DE-1 (EICS)	Polar (TIMAS)	Akebono (SMS)
Data years			1996-08 to 2009-12	1983-02 to 1984-05	1981-09 to 1984-05	1996-04 to 1998-09	1989-10 to 1998-09
Quiet time			$K_p \leq 3$ and 24 hours before initiating of storms	$K_p \leq 3$ 4-dayas after $Dst > -30nT$	$K_p \leq 2$	$0 \leq Kp \leq 7$ With $\overline{K_p} = 2-$	$K_p \leq 2$
Active time			three phases of CME and SIR moderate storms	$3 < K_p \leq 5$	$K_p \geq 3$		$K_p \geq 3$
Altitude(km)			1500-4200	5000-8000	16000-23000	6000-8000	6000-10000
Energy(eV/e)			10-12000	500-16000	10-17000	15-33000	1-70
ILAT			$> 50°$	$> 60°$	$> 56°$	$> 55°$	$> 65°$
Data from Hemisphere(s)			North, South	North, South	North, South	South	North
H^+ rate (s^{-1})	**Solar maximum**	**Active**	2.29×10^{24}		8.5×10^{25}		7×10^{25}
		Quiet	2.63×10^{23}		2.9×10^{25}		3.1×10^{25}
	Solar minimum	**Active**	2.15×10^{24}	3.0×10^{25}	8.5×10^{25}		2.6×10^{25}
		Quiet	2.26×10^{23}	1.1×10^{25}	1.7×10^{25}	2.4×10^{24}	1.5×10^{25}
O^+ rate (s^{-1})	**Solar maximum**	**Active**	4.62×10^{24}		2.4×10^{26}		7.5×10^{25}
		Quiet	5.97×10^{23}		2.1×10^{25}		1.2×10^{25}
	Solar minimum	**Active**	2.15×10^{24}	4.2×10^{25}	8.85×10^{25}		4×10^{24}
		Quiet	1.89×10^{23}	0.27×10^{25}	4.8×10^{25}	3×10^{24}	2.9×10^{23}

604

[1] From observations reported in this paper.
[2] From Table 1. in (Collin et al., 1984).
[3] From Figure 3. in (Yau et al., 1988).
[4] From Table 5. in (Peterson et al., 2001).
[5] From Figure 3. in (Cully et al., 2003)

605 **Figures**

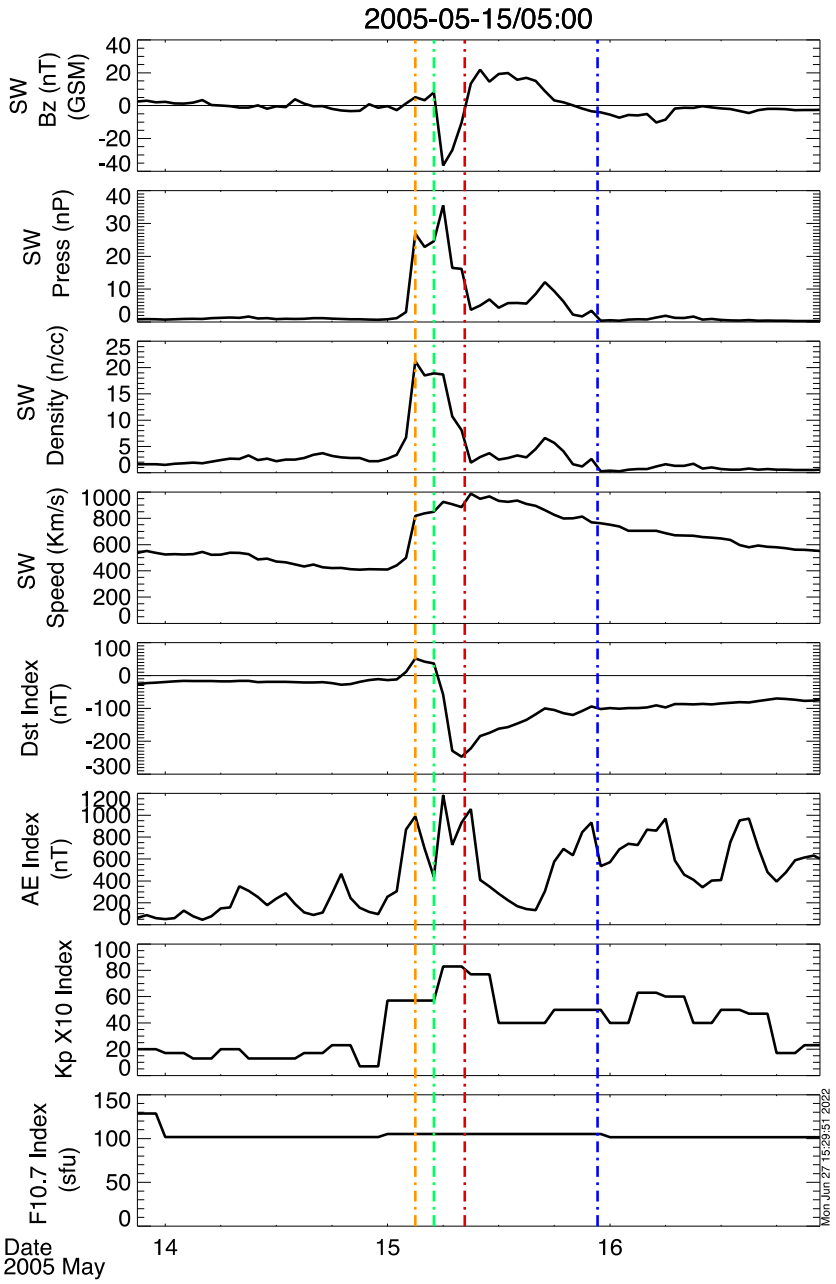

Figure 1. The solar wind parameters during a classical storm. The vertical lines present the storm critical times; the orange line denotes the increase time, the green line shows the onset time, the red line gives the time of minimum Dst, and the blue line recovery time.*

606

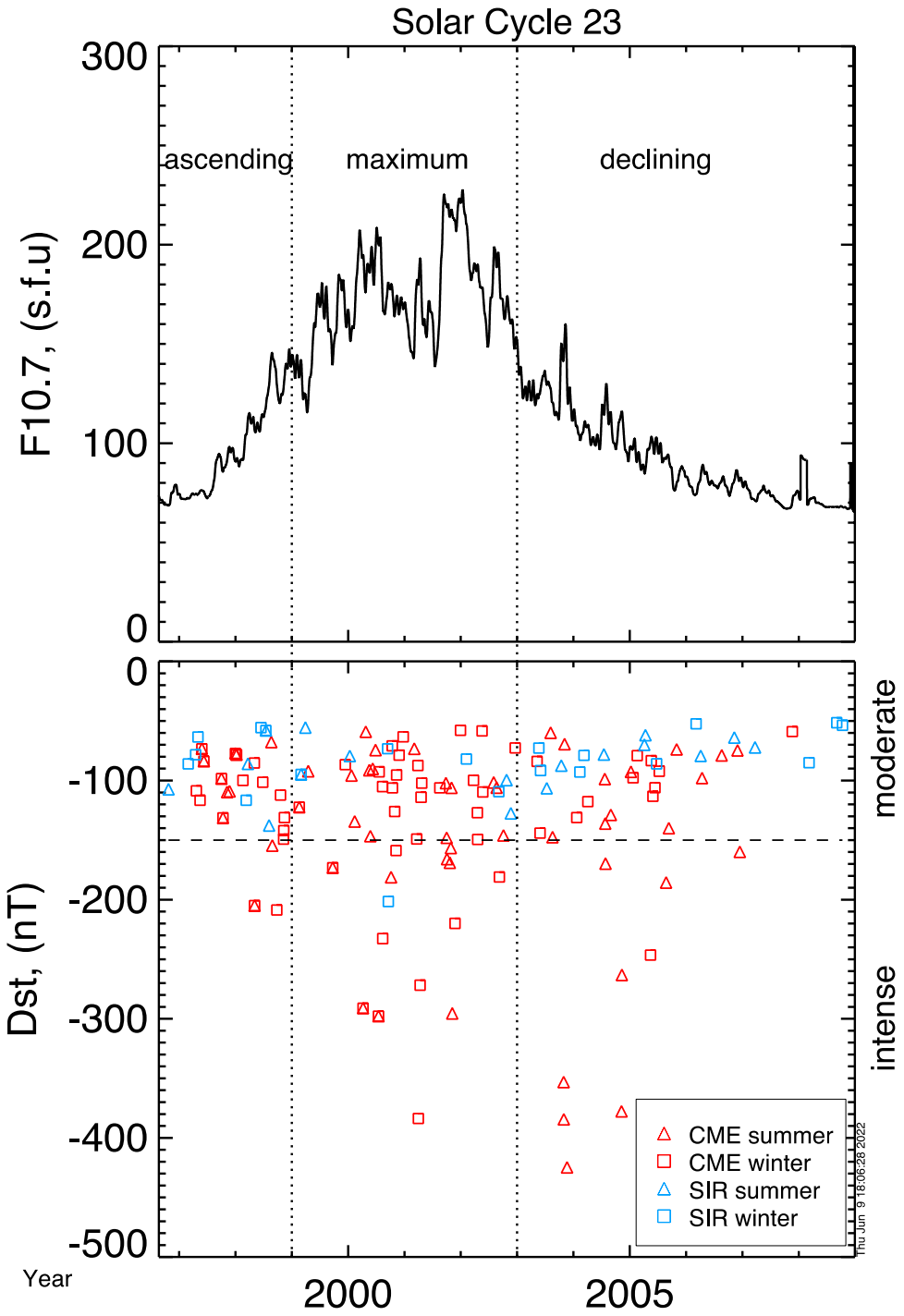

Figure 2. The top panel shows the F10.7 index for solar cycle 23. The vertical lines separate the solar cycle phases. The bottom panel shows the minimum Dst for storms, ICME (red) and SIR (blue). The horizontal dashed line separates the moderate storms from intense storms.

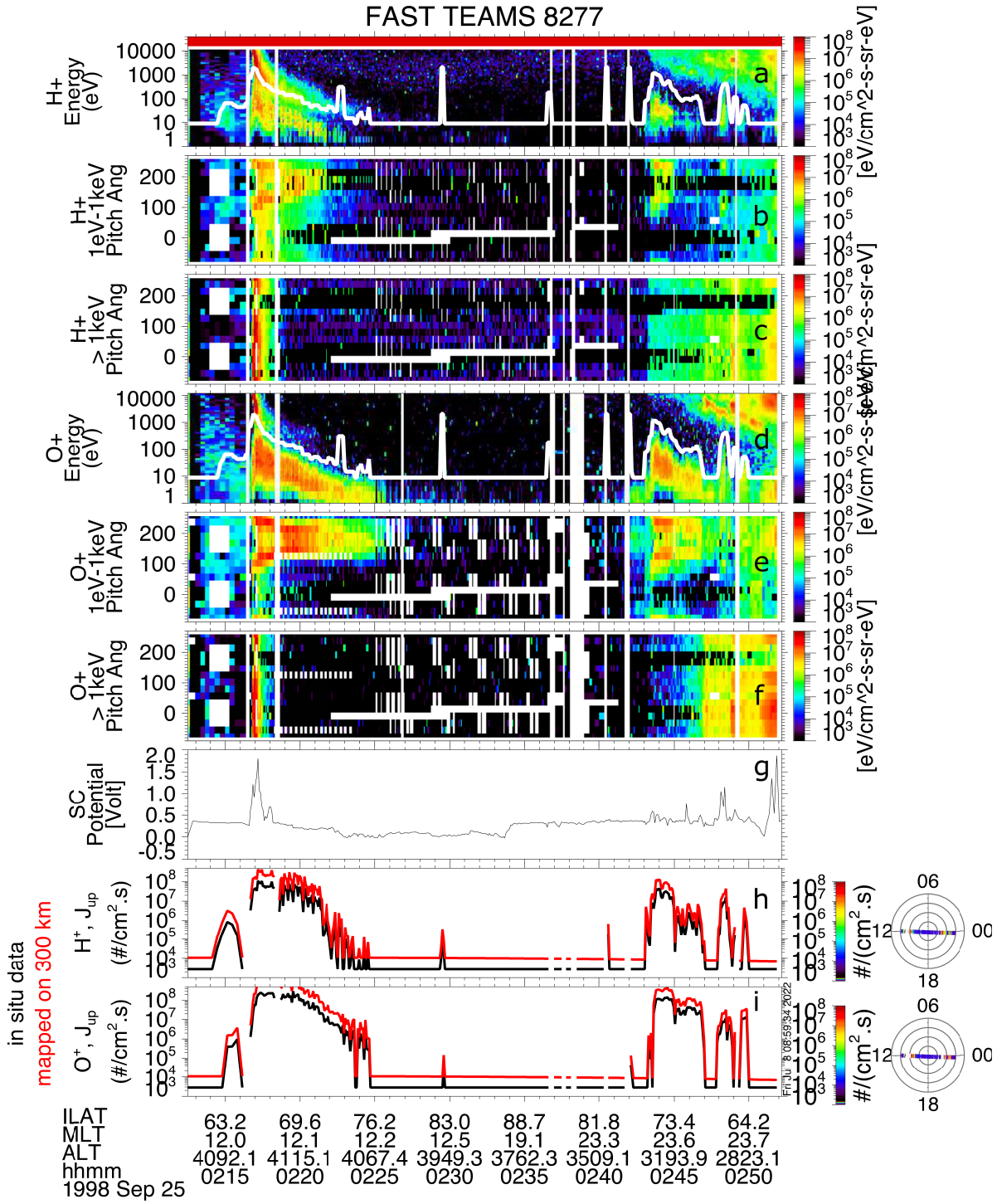

Figure 3. TEAMS summary plot for O^+ and H^+ data from orbit 8277. Panels (a, b, c, h) show the energy spectrogram, pitch angle spectrogram for low energy, pitch angle spectrogram for high energy and in situ outflow flux (black), and mapped outflow flux(red) for H^+ ions. Similar plots for O^+ ions are presented in panels (d, e, f, i). The spacecraft potential is plotted in panel (g). The white lines in panels (a) and (d) represent the upper energy cutoff.

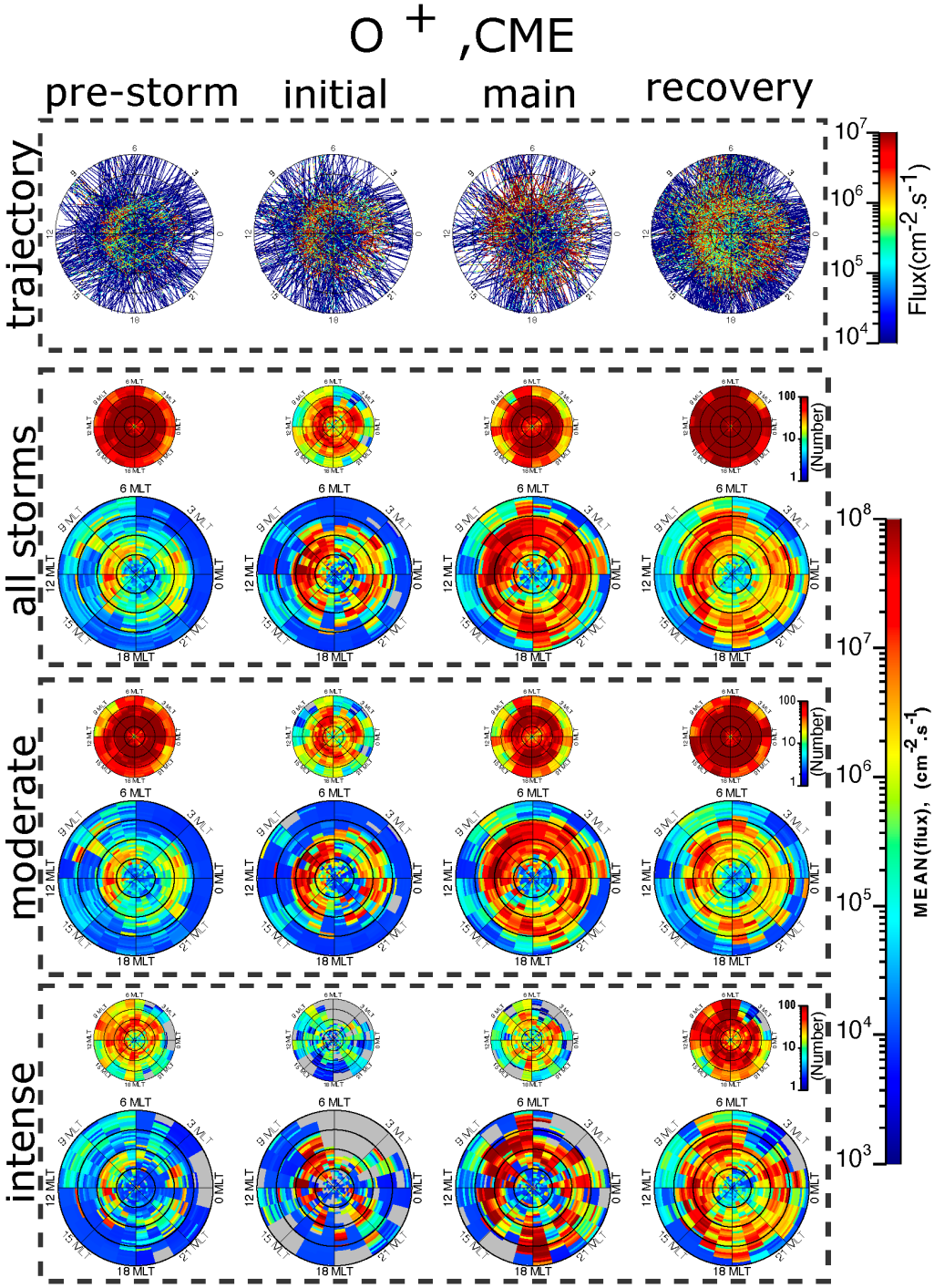

Figure 4. The first row from the top shows the O^+ outflow flux during CME-driven storms along the FAST trajectory before the storm and then for three storm phases. In the second to the fourth row, the big globe plots contain the averaged outflow flux in each MLT-ILAT bin for all classical storms in the second row, for moderate storms with -150 nT ≤ $Dst_{minimum}$ <-50 nT in the third row, and intense storms without $Dst_{minimum}$≤-150 nT in the bottom row. The small globe plots on the top of big plots present the number of data points in each MLT-ILAT bin. The long color bar on the right shows the averaged outflow flux in the bins of big globe plots and three short color bars show the number of data points in each bin of small globe plots.

609

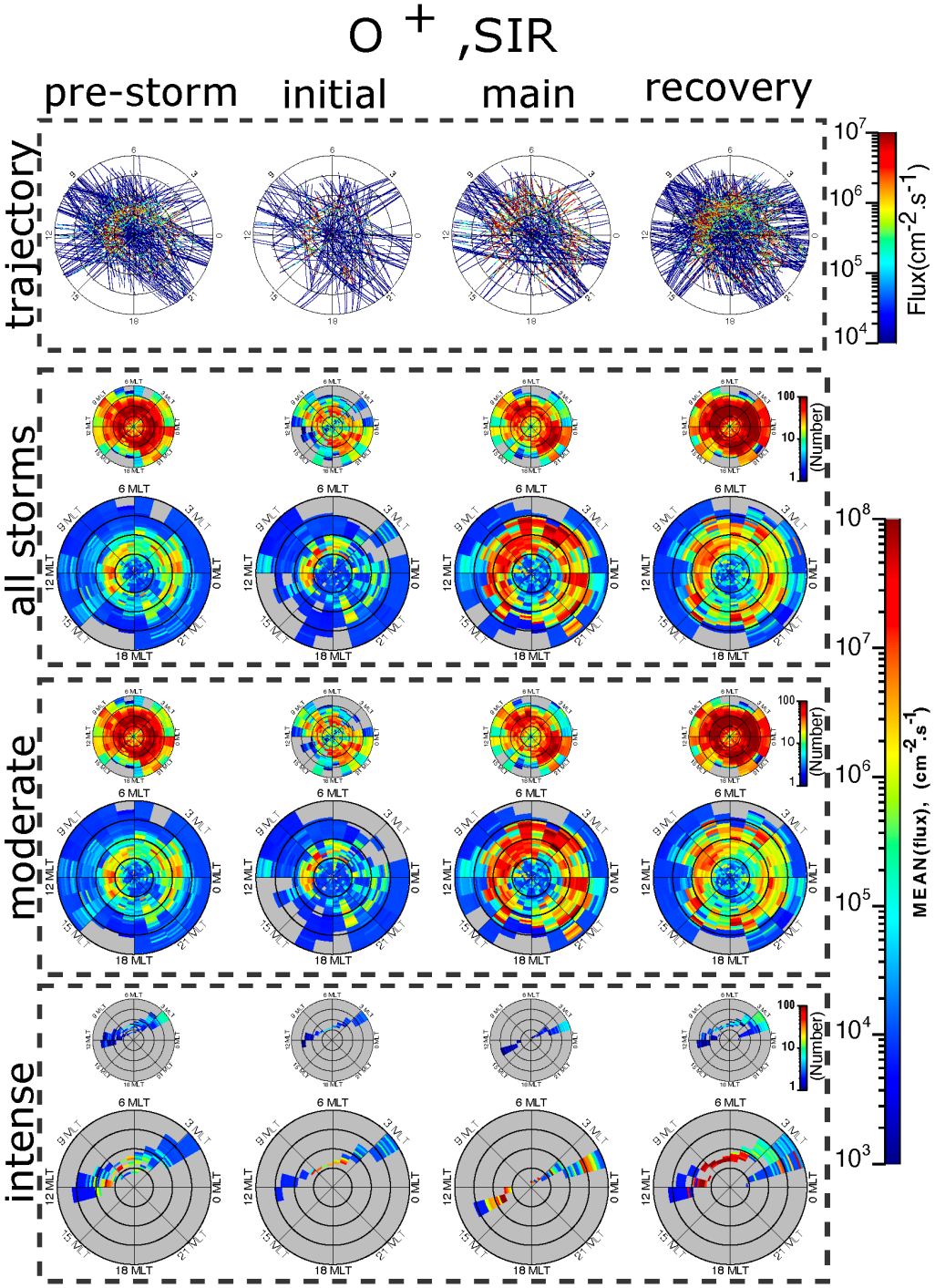

Figure 5. The O^+ outflow flux for SIR-driven storms. The format is the same as for Figure 4.

610

611

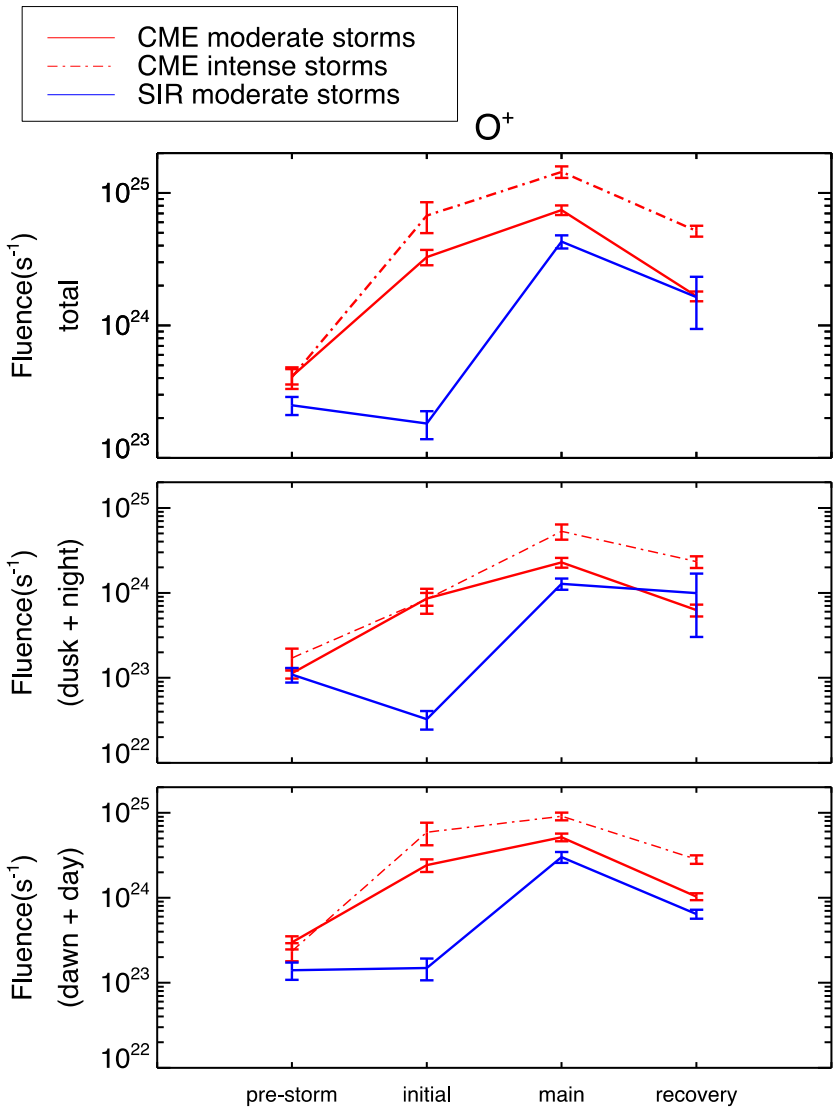

Figure 6. The total O^+ fluence for CME storms in red and SIR storms in blue. The solid lines indicate the fluence during moderate storms and the dashed line during intense storms.

612

613

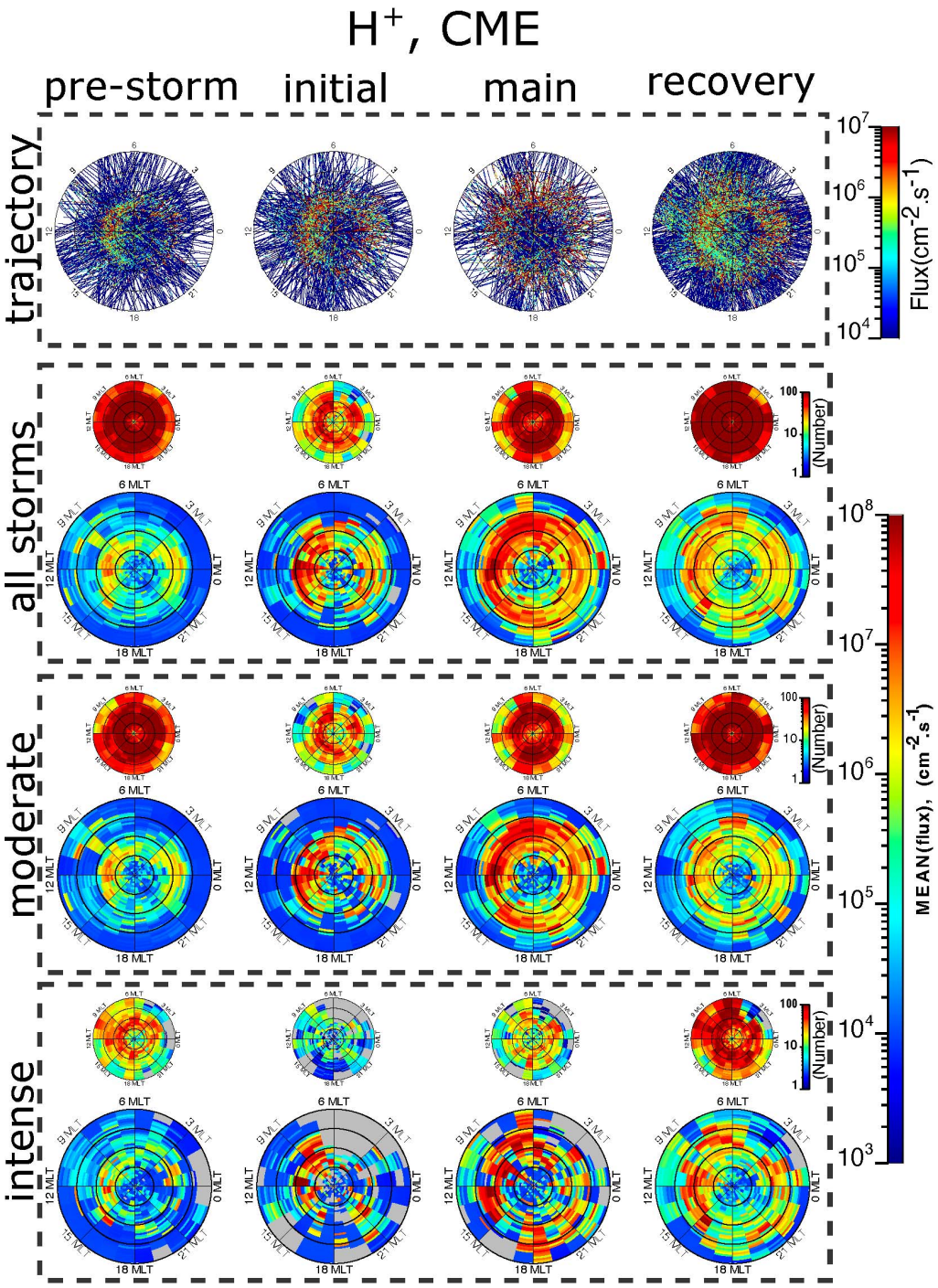

Figure 7. The H^+ outflow flux for CME-driven storms. The format is the same as Figure 4

614

615

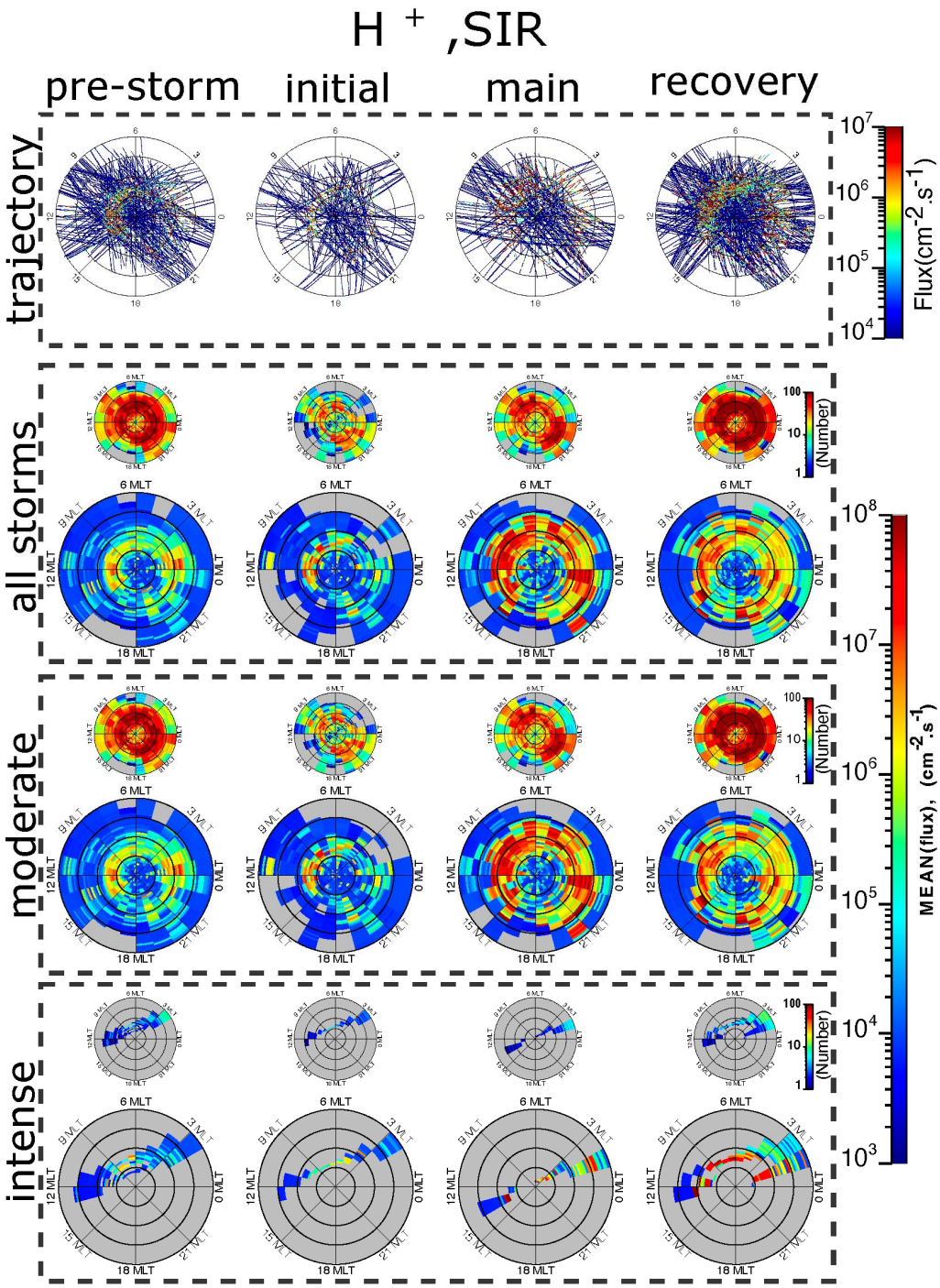

Figure 8. The H^+ outflow flux for SIR-driven storms. The format is the same as in Figure 4.

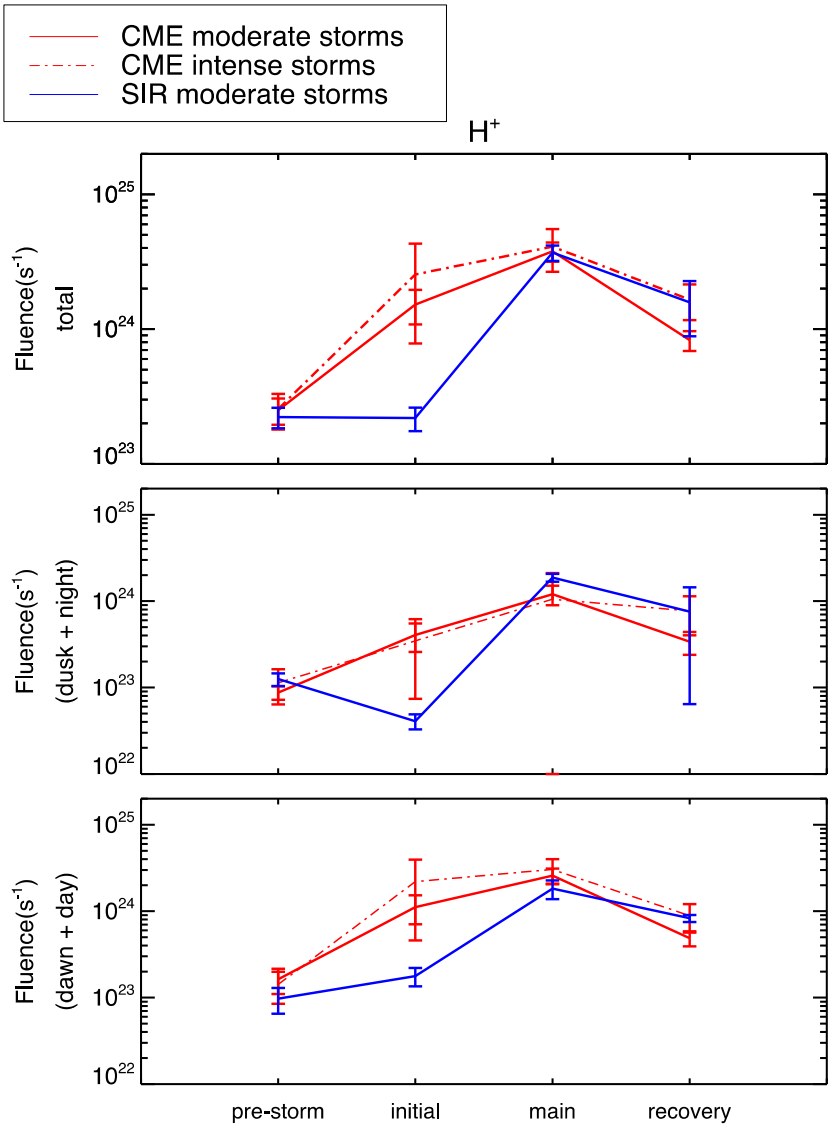

Figure 9. The total H^+ fluence for CME storms in red and SIR storms in blue. The solid lines indicate the fluence during moderate storms and the dashed line during intense storms.

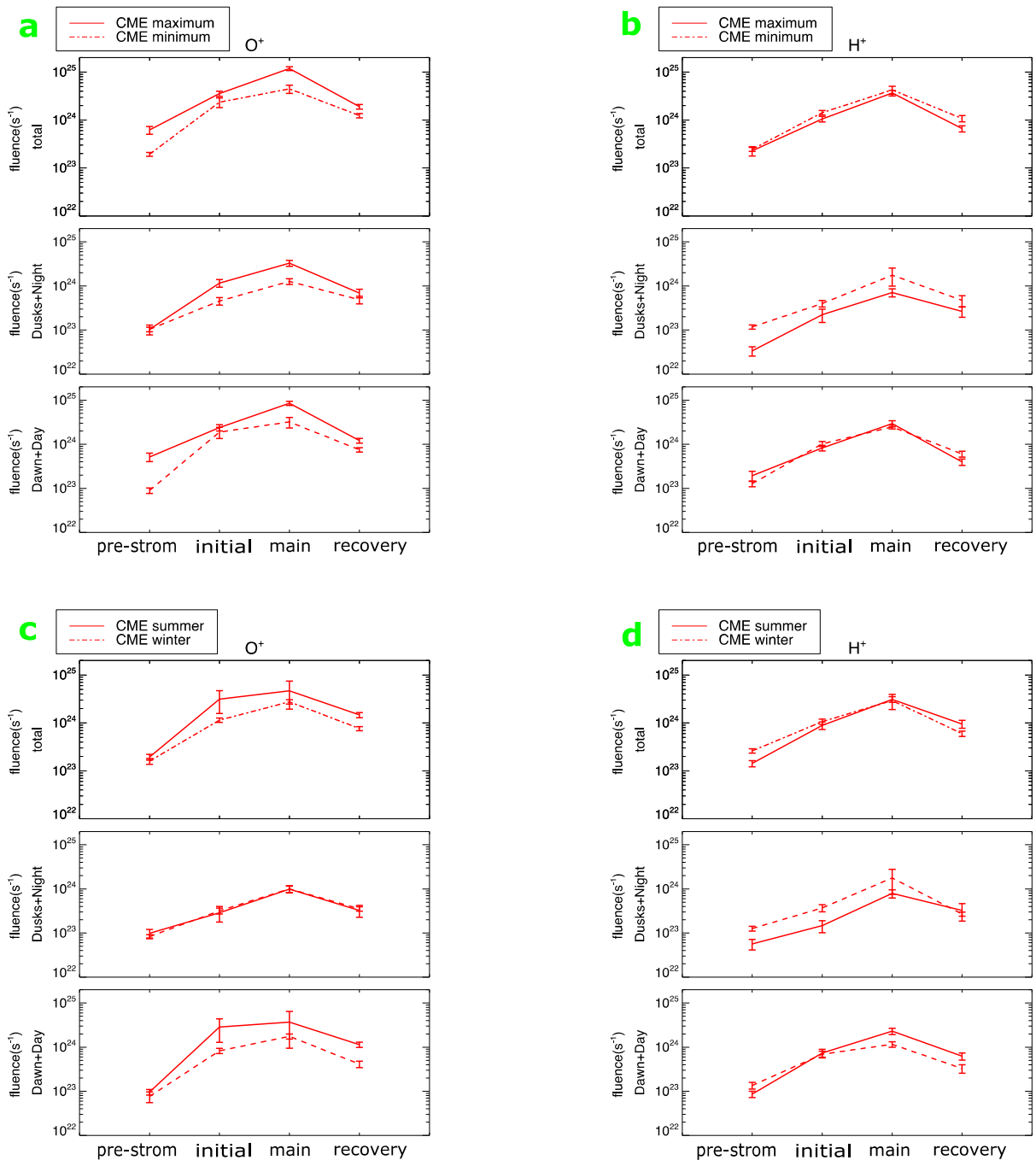

Figure 10. Panel (a, b) show the total O^+ and H^+ fluences for moderate CME storms. The solid lines indicate the fluence during storms of solar maximum years, and the dashed lines during storms of solar minimum. The calculated fluences, separately for (dusk + night) and (dawn + day), are shown in the second and third panels from the top. Panels (c, d) show the O^+ and H^+ fluences for moderate CME storms in solar minimum years. The solid lines indicate the summer season fluence, and the dashed present the winter season fluence. Panels from the top to the bottom are the same as panels (a. b).

619

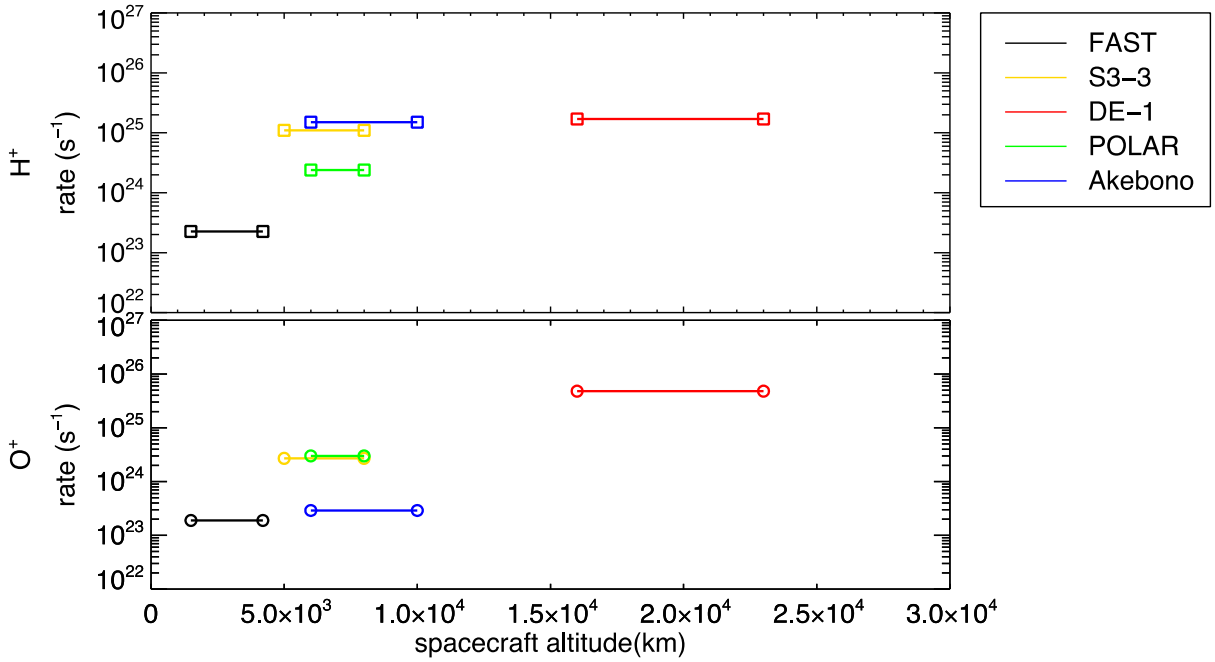

Figure 11. The top and bottom panels present the averaged H^+ and O^+ fluences from various spacecraft at different altitudes. The fluences are from the quiet time of minimum phase rows in Table 2.

Figure 1.

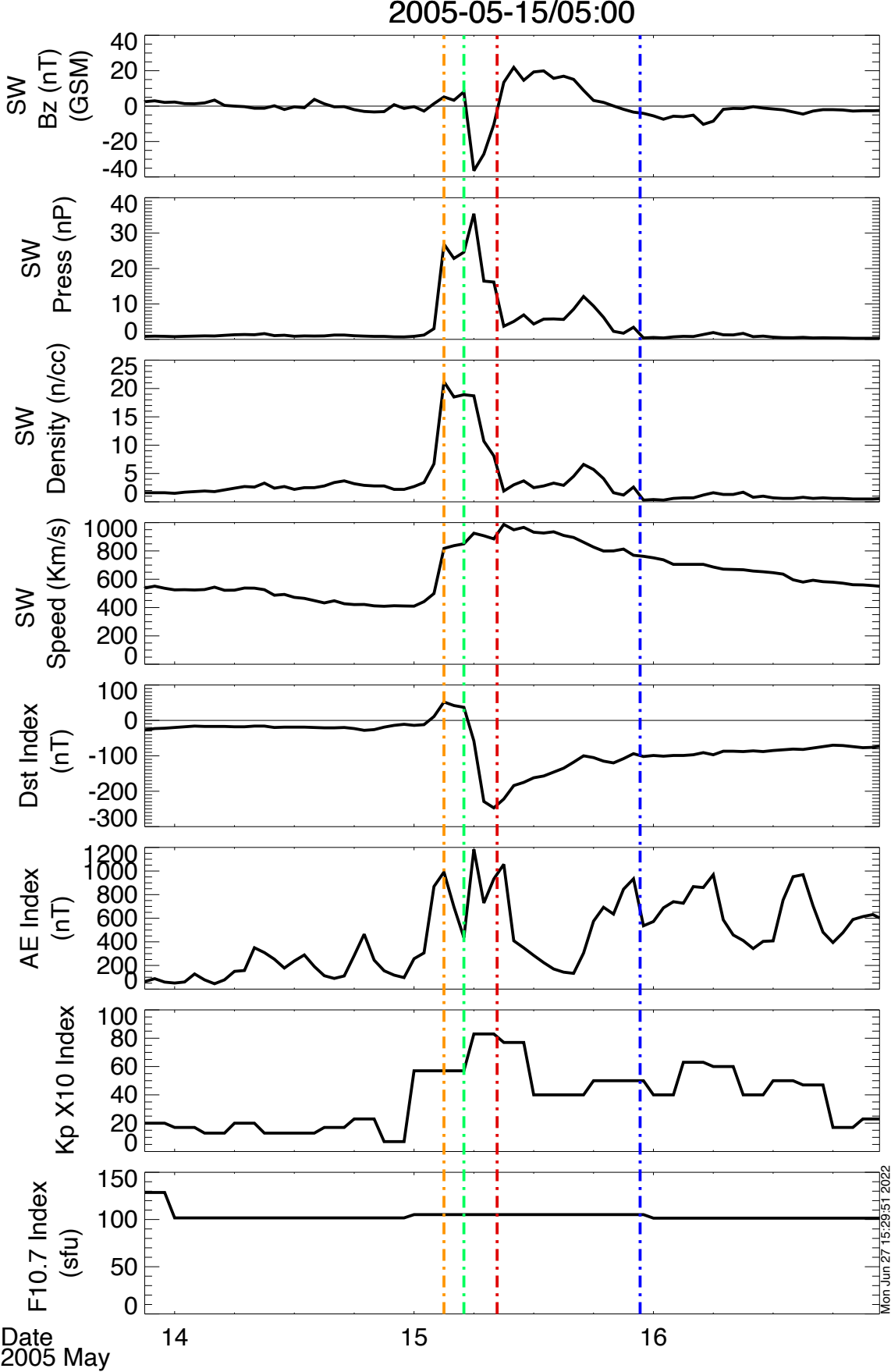
2005-05-15/05:00
SW Bz (nT) (GSM)
SW Press (nP)
SW Density (n/cc)
SW Speed (Km/s)
Dst Index (nT)
AE Index (nT)
Kp X10 Index
F10.7 Index (sfu)
Date 2005 May
14
15
16
Mon Jun 27 15:29:51 2022

Figure 2.

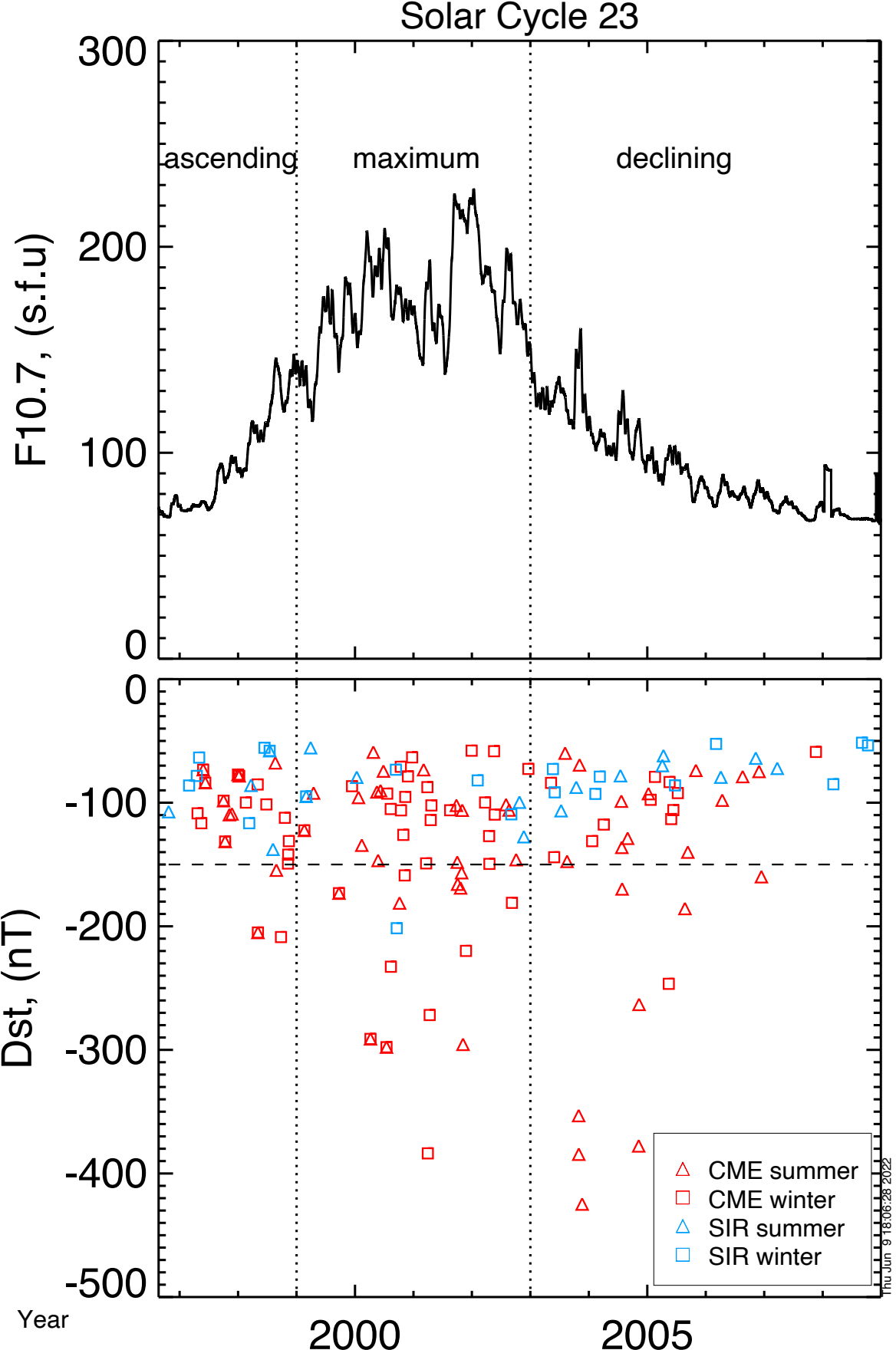
Solar Cycle 23
ascending
maximum
declining
F10.7, (s.f.u)
300
200
100
0
Dst, (nT)
0
-100
-200
-300
-400
-500
moderate
intense
CME summer
CME winter
SIR summer
SIR winter
Year
2000
2005
Thu Jun 9 18:06:28 2022

Figure 3.

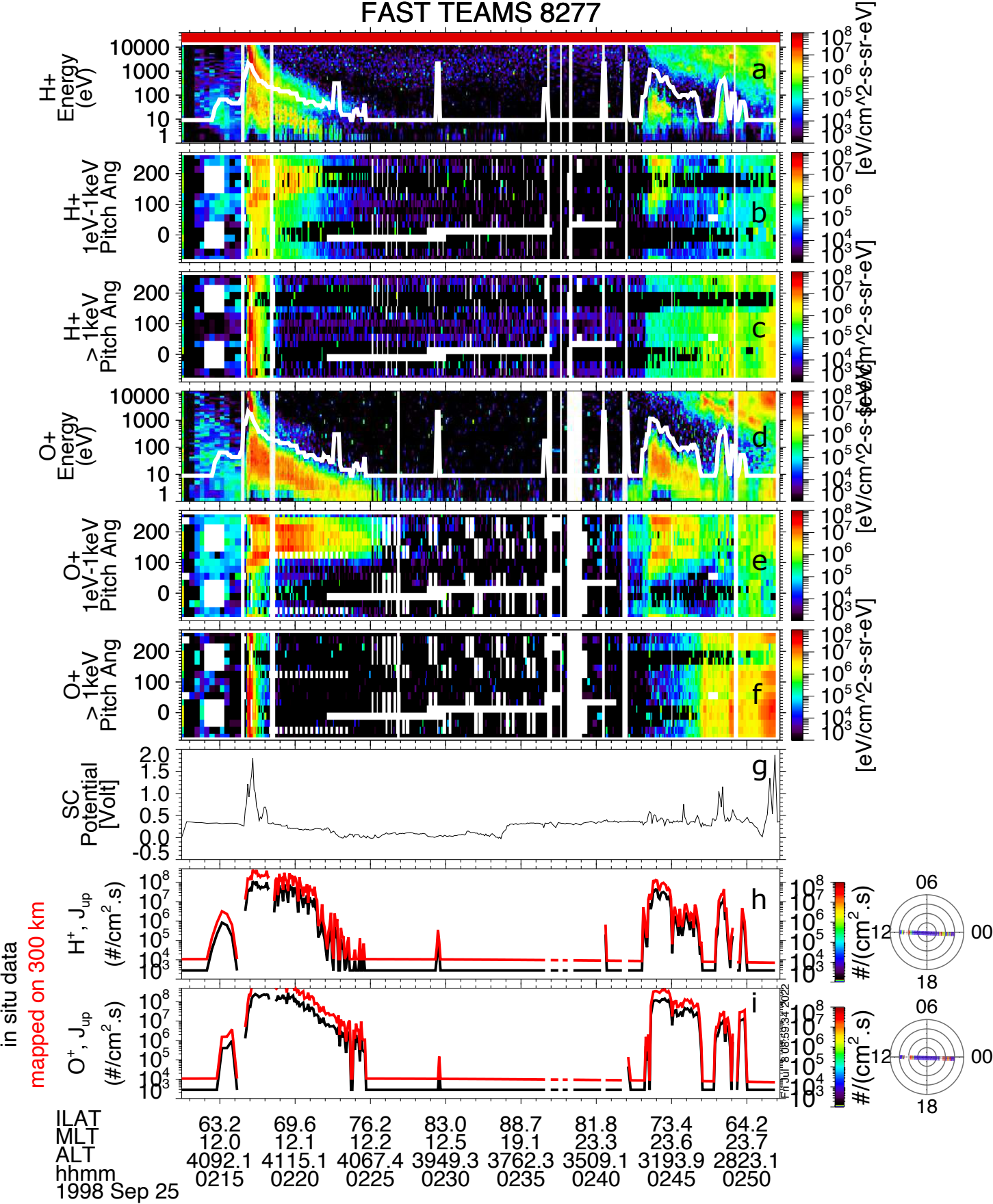
FAST TEAMS 8277
H+ Energy (eV)
a
H+ 1eV-1keV Pitch Ang
b
H+ >1keV Pitch Ang
c
O+ Energy (eV)
d
O+ 1eV-1keV Pitch Ang
e
O+ >1keV Pitch Ang
f
[eV/cm^2-s-sr-eV]
SC Potential [Volt]
g
H+, Jup (#/cm2.s)
h
O+, Jup (#/cm2.s)
i
#/(cm2.s)
06
12
00
18
Fri Jul 8 08:59:34 2022
in situ data
mapped on 300 km
ILAT 63.2 69.6 76.2 83.0 88.7 81.8 73.4 64.2
MLT 12.0 12.1 12.2 12.5 19.1 23.3 23.6 23.7
ALT 4092.1 4115.1 4067.4 3949.3 3762.3 3509.1 3193.9 2823.1
hhmm 0215 0220 0225 0230 0235 0240 0245 0250
1998 Sep 25

Figure 4.

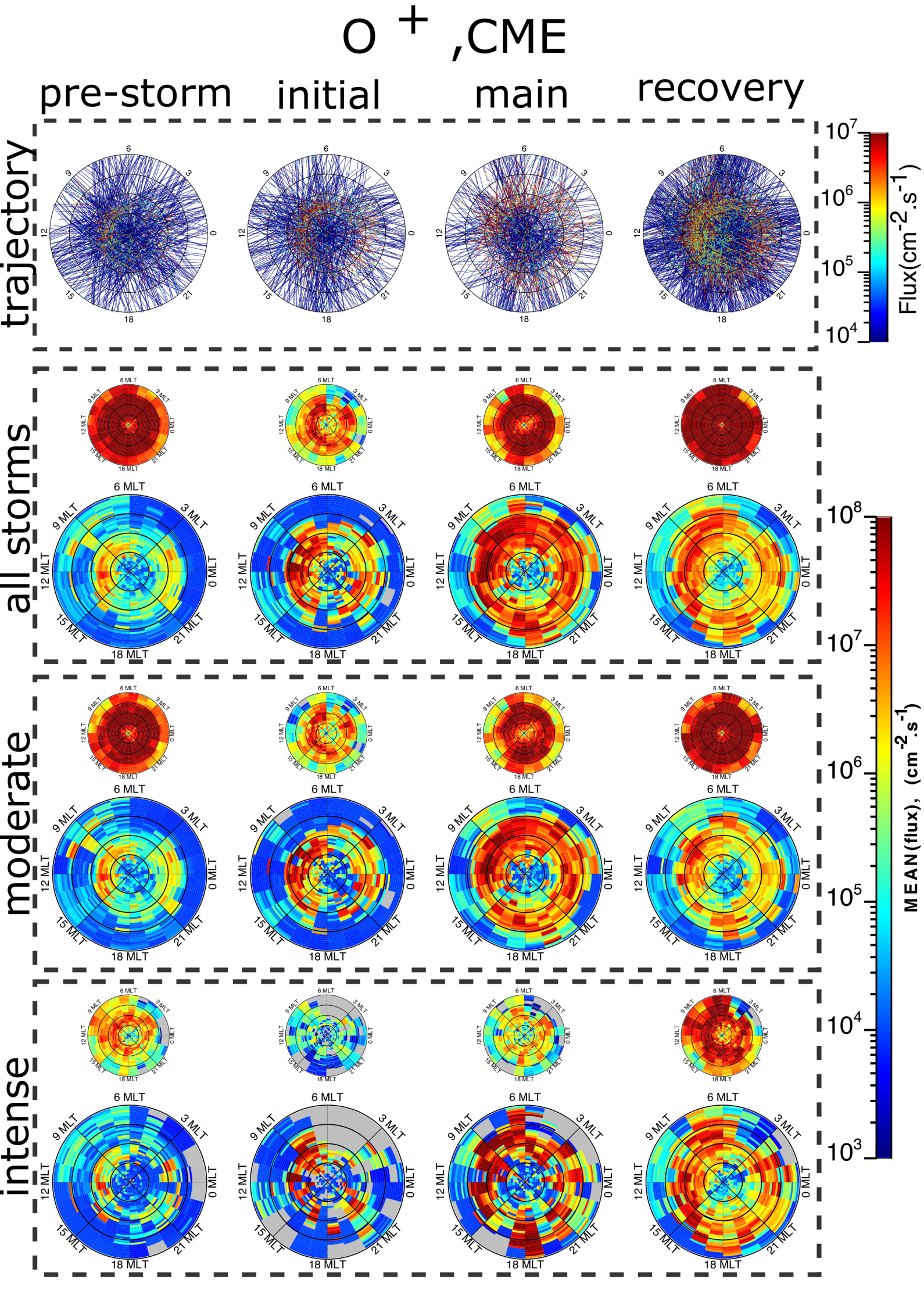
O +,CME
pre-storm
initial
main
recovery
trajectory
all storms
moderate
intense
6
9
3
12
0
15
18
21
6 MLT
3 MLT
0 MLT
9 MLT
12 MLT
15 MLT
18 MLT
21 MLT
10^7
10^6
10^5
10^4
Flux(cm^{-2}.s^{-1})
10^8
10^7
10^6
10^5
10^4
10^3
MEAN(flux), (cm^{-2}.s^{-1})

Figure 5.

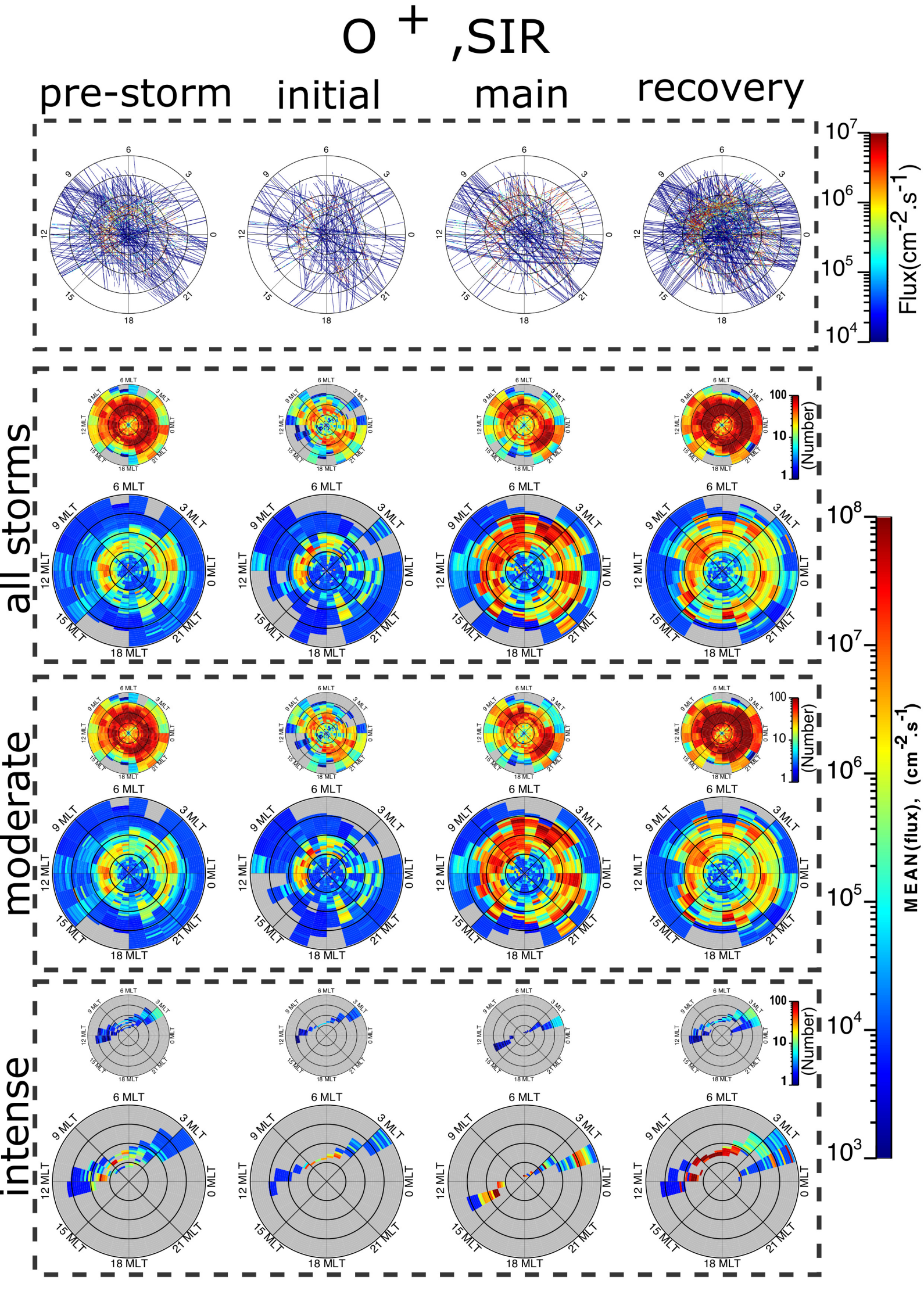
O +,SIR
pre-storm
initial
main
recovery
all storms
moderate
intense
6 MLT
3 MLT
0 MLT
21 MLT
18 MLT
15 MLT
12 MLT
9 MLT
Flux(cm-2.s-1)
(Number)
MEAN(flux), (cm-2.s-1)

Figure 6.

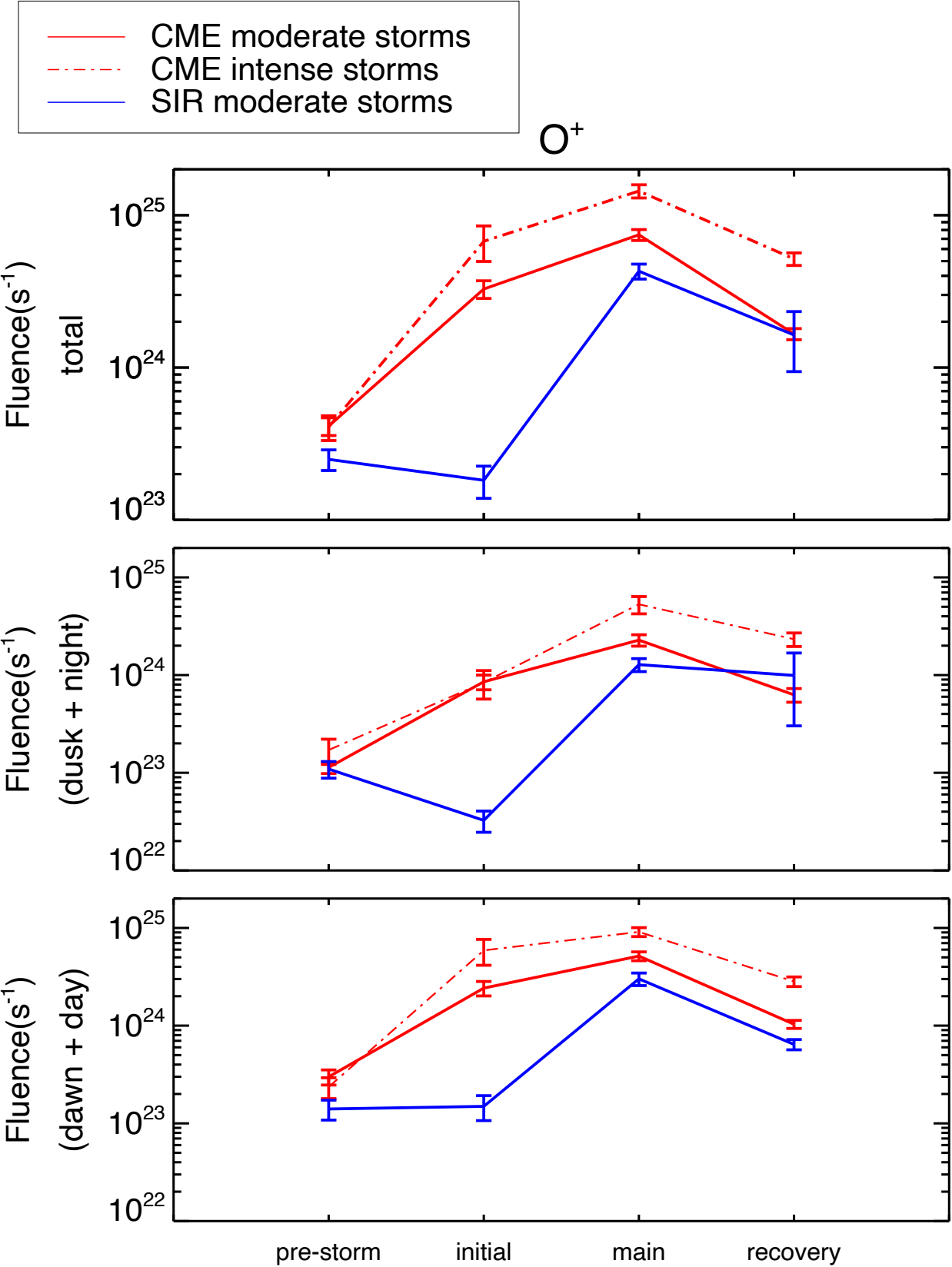
CME moderate storms
CME intense storms
SIR moderate storms
O+
Fluence(s-1)
total
(dusk + night)
(dawn + day)
10^25
10^24
10^23
10^22
pre-storm
initial
main
recovery

Figure 7.

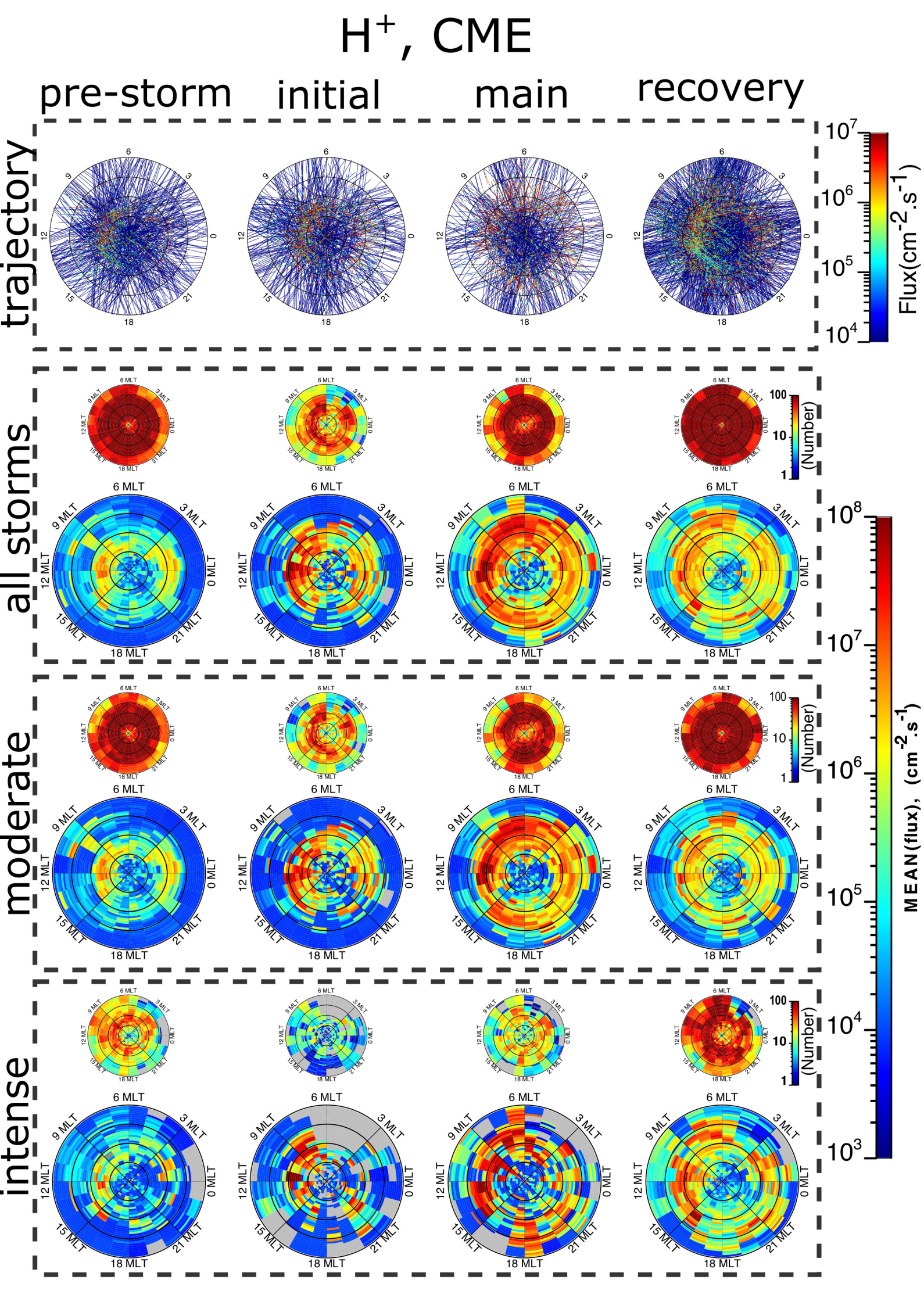
H+, CME
pre-storm
initial
main
recovery
trajectory
all storms
moderate
intense
Flux(cm-2.s-1)
(Number)
MEAN(flux), (cm-2.s-1)
6 MLT
3 MLT
0 MLT
21 MLT
18 MLT
15 MLT
12 MLT
9 MLT

Figure 8.

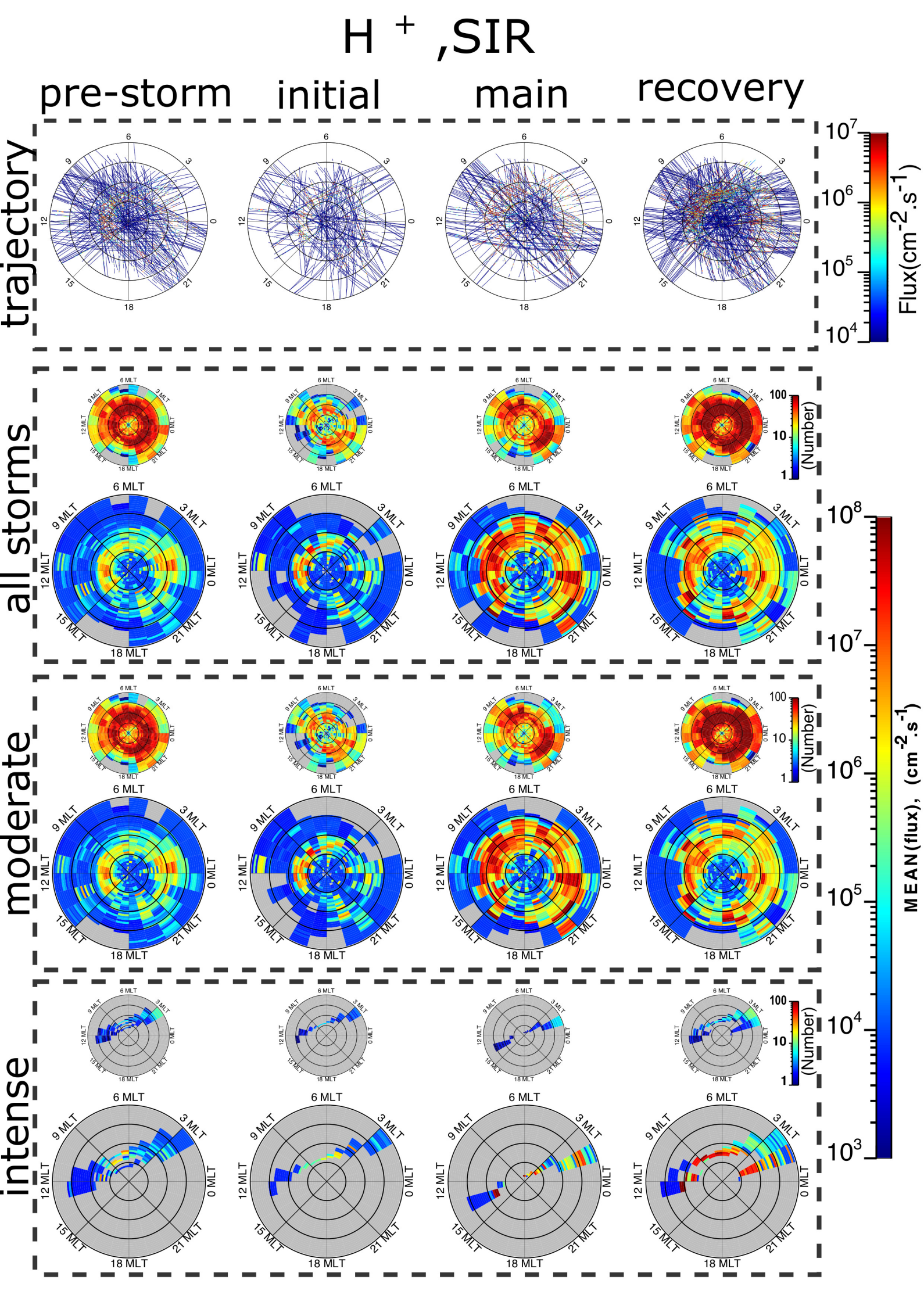
H + ,SIR
pre-storm
initial
main
recovery
trajectory
all storms
moderate
intense
Flux(cm-2.s-1)
(Number)
MEAN(flux), (cm-2.s-1)
6 MLT
9 MLT
3 MLT
12 MLT
0 MLT
15 MLT
21 MLT
18 MLT

Figure 9.

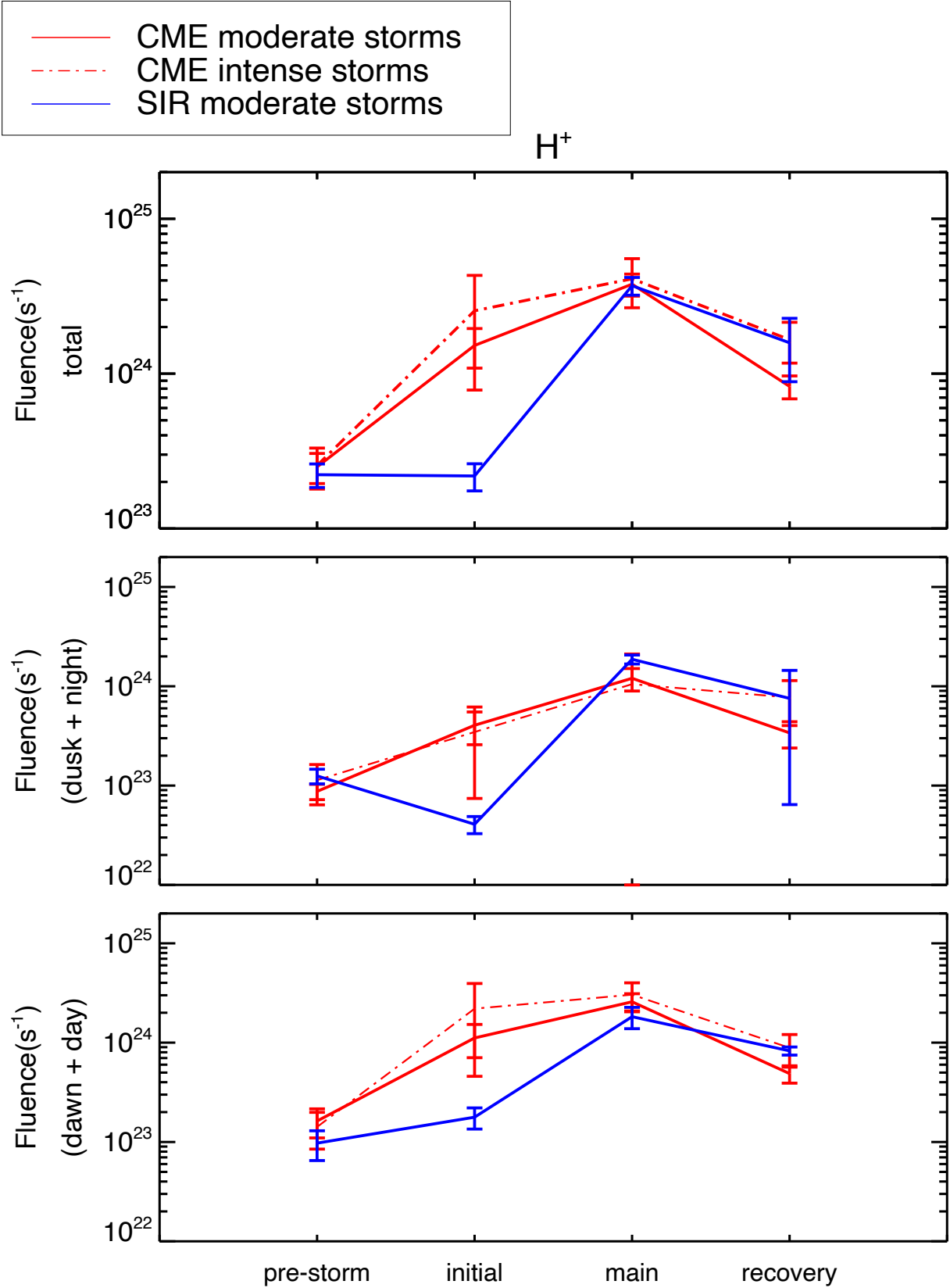
CME moderate storms
CME intense storms
SIR moderate storms
H+
Fluence(s-1)
total
(dusk + night)
(dawn + day)
10^25
10^24
10^23
10^22
pre-storm
initial
main
recovery

Figure 10.

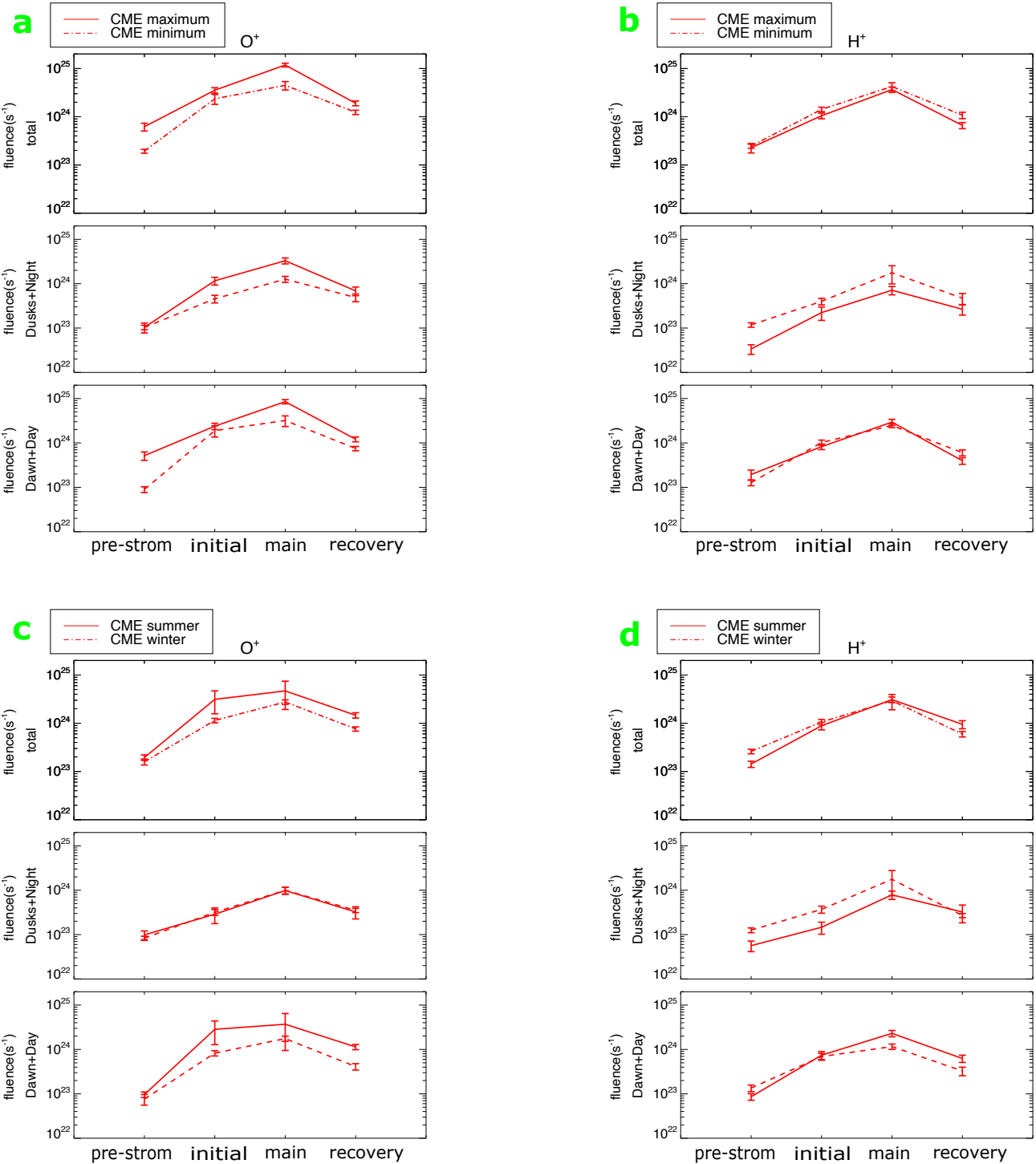
a
CME maximum
CME minimum
O+
b
CME maximum
CME minimum
H+
c
CME summer
CME winter
O+
d
CME summer
CME winter
H+
fluence(s-1)
total
Dusks+Night
Dawn+Day
10^25
10^24
10^23
10^22
pre-strom
initial
main
recovery

Figure 11.

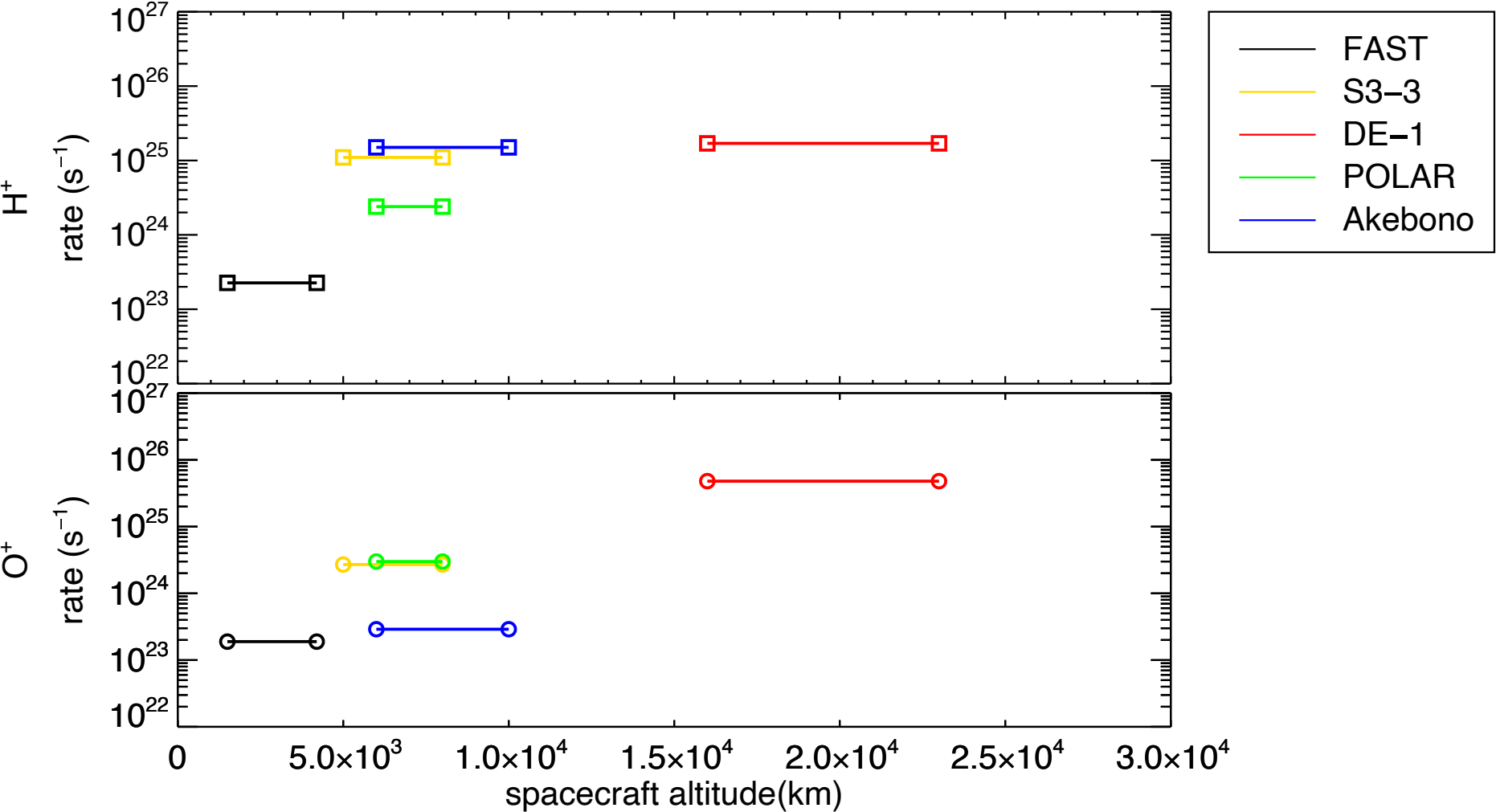
H+
O+
rate (s−1)
rate (s−1)
10^27
10^26
10^25
10^24
10^23
10^22
0
5.0×10^3
1.0×10^4
1.5×10^4
2.0×10^4
2.5×10^4
3.0×10^4
spacecraft altitude(km)
FAST
S3–3
DE–1
POLAR
Akebono

Table 1. Geomagnetic storms with identified drivers from 1996 to 2008.

	TOTAL	**CME**	**SIR**
total storms	139	104	35
intense storm(I-storms)	27	26	1
moderate storm(M-storms)	112	78	34
M-storm in maximum phase	45	37	8
		Summer: 15	Summer: 4
		Winter: 21	Winter: 3
		Summer and winter: 1	Summer and winter: 1
M- storm in minimum phase	67	41	26
		Summer: 15	Summer: 11
		Winter: 20	Winter: 14
		Summer and winter: 6	Summer and winter: 1

Table 2. Comparing the total H^+ and O^+ fluences scaping from ionosphere in different studies.

			This Study[1]	**Collin**[2]	**Yau**[3]	**Peterson**[4]	**Cully**[5]
Spacecraft			FAST (TEAMS)	S3-3 (Lockheed)	DE-1 (EICS)	Polar (TIMAS)	Akebono (SMS)
Data years			1996-08 to 2009-12	1983-02 to 1984-05	1981-09 to 1984-05	1996-04 to 1998-09	1989-10 to 1998-09
Quiet time			$K_p \leq 3$ and 24 hours before initiating of storms	$K_p \leq 3$ 4-dayas after $Dst > -30nT$	$K_p \leq 2$	$0 \leq Kp \leq 7$ With $\overline{K_p} = 2 -$	$K_p \leq 2$
Active time			three phases of CME and SIR moderate storms	$3 < K_p \leq 5$	$K_p \geq 3$		$K_p \geq 3$
Altitude(km)			1500-4200	5000-8000	16000-23000	6000-8000	6000-10000
Energy(eV/e)			10-12000	500-16000	10-17000	15-33000	1-70
ILAT			$> 50°$	$> 60°$	$> 56°$	$> 55°$	$> 65°$
Data from Hemisphere(s)			North, South	North, South	North, South	South	North
H^+ rate (s^{-1})	**Solar maximum**	**Active**	2.29×10^{24}		8.5×10^{25}		7×10^{25}
		Quiet	2.63×10^{23}		2.9×10^{25}		3.1×10^{25}
	Solar minimum	**Active**	2.15×10^{24}	3.0×10^{25}	8.5×10^{25}		2.6×10^{25}
		Quiet	2.26×10^{23}	1.1×10^{25}	1.7×10^{25}	2.4×10^{24}	1.5×10^{25}
O^+ rate (s^{-1})	**Solar maximum**	**Active**	4.62×10^{24}		2.4×10^{26}		7.5×10^{25}
		Quiet	5.97×10^{23}		2.1×10^{25}		1.2×10^{25}
	Solar minimum	**Active**	2.15×10^{24}	4.2×10^{25}	8.85×10^{25}		4×10^{24}
		Quiet	1.89×10^{23}	0.27×10^{25}	4.8×10^{25}	3×10^{24}	2.9×10^{23}

[1] From observations reported in this paper.
[2] From Table 1. in (Collin et al., 1984).
[3] From Figure 3. in (Yau et al., 1988).
[4] From Table 5. in (Peterson et al., 2001).
[5] From Figure 3. in (Cully et al., 2003)